Project No.: 295153

Room-temperature seismic attenuator for the underground interferometer KAGRA and ET perspective

WP1 24 months mid–term report

ET–0008A–14

Rev.04

R. DeSalvo[1], K. Agatsuma[2], F. Pena Arellano[3], A. Bertolini[2], E. Hennes[2], E. Majorana[4], I. Pinto[1], T. Sekiguchi[5], R. Takahashi[3], J. van Heijningen[2] and J. van den Brand[2]

[1]Universitá del Sannio, Benevento, Italy
[2]Nikhef, Amsterdam, The Netherlands
[3]NAOJ, Tokyo, Japan
[4]Universitá La Sapienza, Roma, Italy
[5]University of Tokyo, Japan

March 8, 2014

Contents

1 Introduction

KAGRA is the first large-scale interferometer installed in underground environment to take advantage of low seismic noise conditions for improving the sensitivity in the low frequency band. The microseismic climate in the Kamioka mine (see Fig. 1) would also be compliant with the site requirements for the Einstein Telescope [1]. Multistage vibration isolators will be used for core and ancillary optics to lower the seismic noise disturbance well below the level of all other relevant noise sources, namely the suspension thermal noise from 5 to 30 Hz and quantum noise (radiation pressure and shot noise) at higher frequencies.

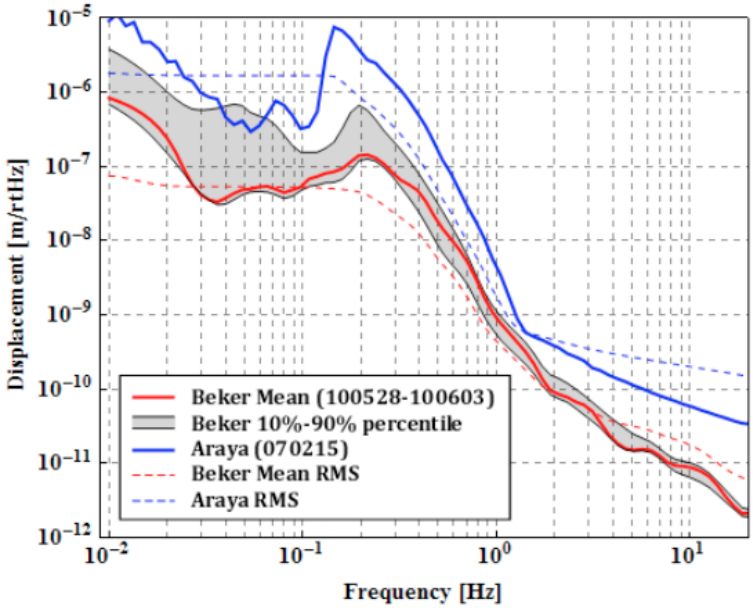

Figure 1: *Seismic noise at KAGRA site. M. Beker (Nikhef) measured Kamioka seismic spectrum in 2010, using a Trillium 240 seismometer. Araya (Univ. of Tokyo) measured the spectrum in 2007 with a Guralp CMG-3 seismometer on an extremely stormy day.*

Different configurations, but using the same components and similar topology, will be adopted for the attenuation chains of payloads at room temperature, so–called Type–B [2], and payloads at cryogenic temperature (the test masses), so–called Type–A [3]. Stacks of the same kind used in TAMA300 [4] (so–called Type–C) will be used for the input mode cleaner, for ancillary optics and automatic alignment sensors. The disposition of KAGRA's suspended mirrors is illustrated in Fig. 2.

The focus of this report is to illustrate the design choices and preliminary

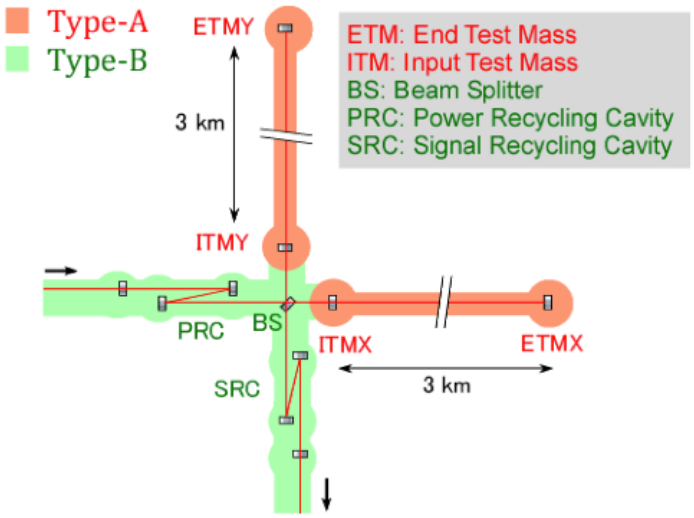

Figure 2: *Layout of the KAGRA suspended mirrors and seismic attenuation system. Type–B SAS is used for beam splitter, power recycling telescope mirror and signal recycling telescope mirrors. Type–A SAS is used for the four cryogenic test masses.*

testing of the Seismic Attenuation System of KAGRA, called KAGRA–SAS. In particular, the conceptual design of Type–B chains, including the warm mirror suspensions, is analyzed. Topology and strategy of controls are presented together with the results of preliminary tests. Design constraints and issues in interfacing the Type–A chains with a cryogenic payload are also discussed. Young scientists from European research institutions contributed, in the framework of the Elites program, to technical design aspects and to the various experimental activities.

2 Attenuator topology and technology background

KAGRA shares with Virgo [5] and TAMA300 [6] the philosophy of passive seismic attenuation chains, each suspending a main optical component. The use of large vacuum chambers and optical tables suspending several components, including main optics is avoided. This choice lends much greater flexibility to the facility, at a much reduced cost.

The design of KAGRA's seismic attenuation and mirror suspension has a long and solid pedigree. Its isolation and control scheme topology is derived from the very successful Virgo Superattenuators (Fig. 3) [7], which were later, in a simplified version, adopted in TAMA300 (so–called TAMA–

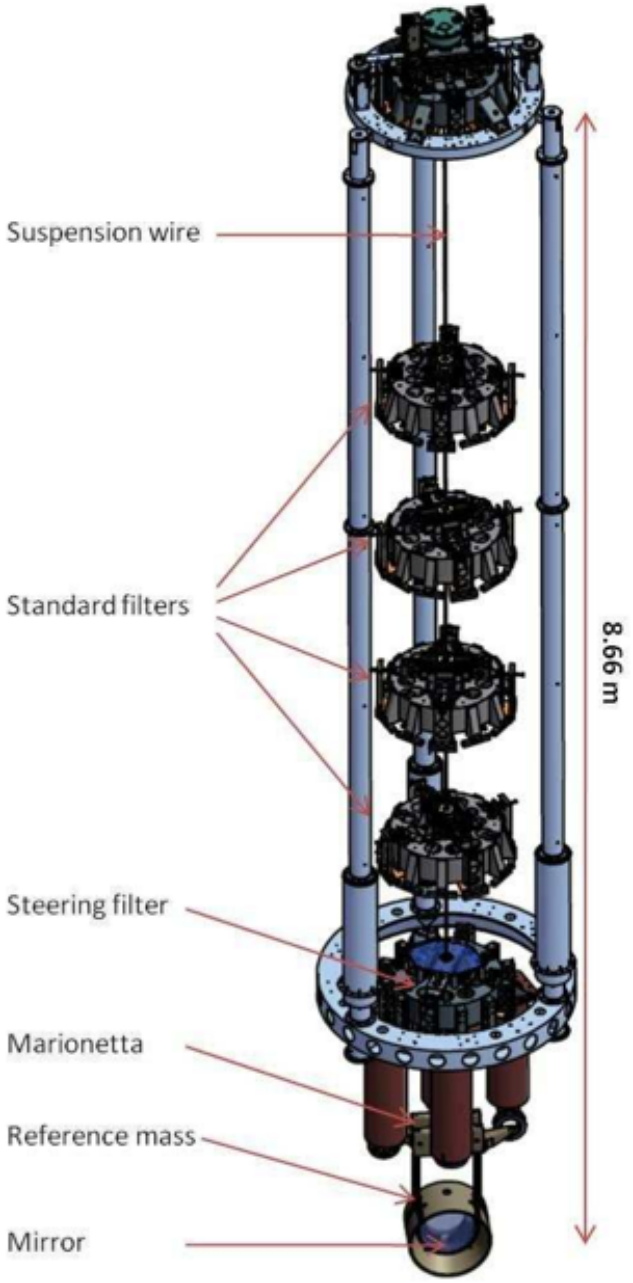

Figure 3: *The Virgo superattenuator: the mechanical filter chain adopted to attenuate seismic vibration in the detection band, the three-leg inverted pendulum preisolator, the top filter of the chain (so-called F0) and the payload are well visible. The inertial damping acts on the top stage to compensate tidal motion and any slow drift motion so that to reduce the mirror swinging within the detection bandwidth (above 10 Hz).*

SAS [8] [9]). KAGRA, although topologically almost identical to its predecessors Virgo and TAMA, uses more advanced filtering elements [10]. KAGRA's design incorporates the latest techniques to mitigate or eliminate drawbacks encountered in the preceding systems listed above. Like Virgo's and TAMA's, KAGRA's attenuation chains are composed by:

- a four degrees-of-freedom (two horizontal translations, yaw and vertical) passive very low frequency pre–isolator, optimized for performance augmentation by means of optional active attenuation, if needed;
- a chain composed of a variable number of passive standard isolation filters each providing attenuation along all six degrees-of-freedom;
- a mirror suspension and control scheme based on an upper level control applied on an intermediate mass from the last filter of the chain (named bottom filter) and the marionette concept with concentric recoil masses for dynamic mirror control.

The 13 m tall seismic attenuation chains isolating the four main cryogenic mirrors of KAGRA are called Type–A. Each extends between two superimposed tunnels and is composed by a pre–isolator, three standard filters, and a control filter supporting the optical payload, providing the dynamic controls needed to acquire lock. They are illustrated in Fig. 4 left panel.

The 3–m tall seismic attenuation chains suspending the beam splitter mirror and the six recycler mirrors (three for the power recycler arm, and three for the signal recycler arm) are called Type–B and comprise only one standard filter (instead of three), matching the less stringent isolation requirements. Apart from the number of filters and length, they are topologically identical and functionally similar to the type-A chains. They are illustrated in Fig. 4 right panel. The components of the attenuation chains of both types are common (engineering details are in [3][2][12]). KAGRA–SAS shares the same technologies and many of the components with the seismically isolated tables of the AEI 10–m prototype interferometer (AEI-SAS) [13], the Advanced Virgo seismic isolator for the external injection bench (EIB–SAS) [14] and the Advanced Virgo multistage seismic isolators (Multi–SAS) for the auxiliary optics suspended benches [15]. Main building blocks are:

Geometric Anti–Spring (GAS) filters A GAS spring (see Fig. 5) [16]is a set of radially arranged cantilever *blades* mounted from a common retainer structure (*body*) and opposing each other via a central disk (*keystone*), to which the payload to be isolated is connected.

The blades are completely flat when manufactured and flex like a fishing rod under load (see Fig. 6). Suitable clamps provide the blade base an initial angle of 45° to accommodate the bending. On the other side the blade tip

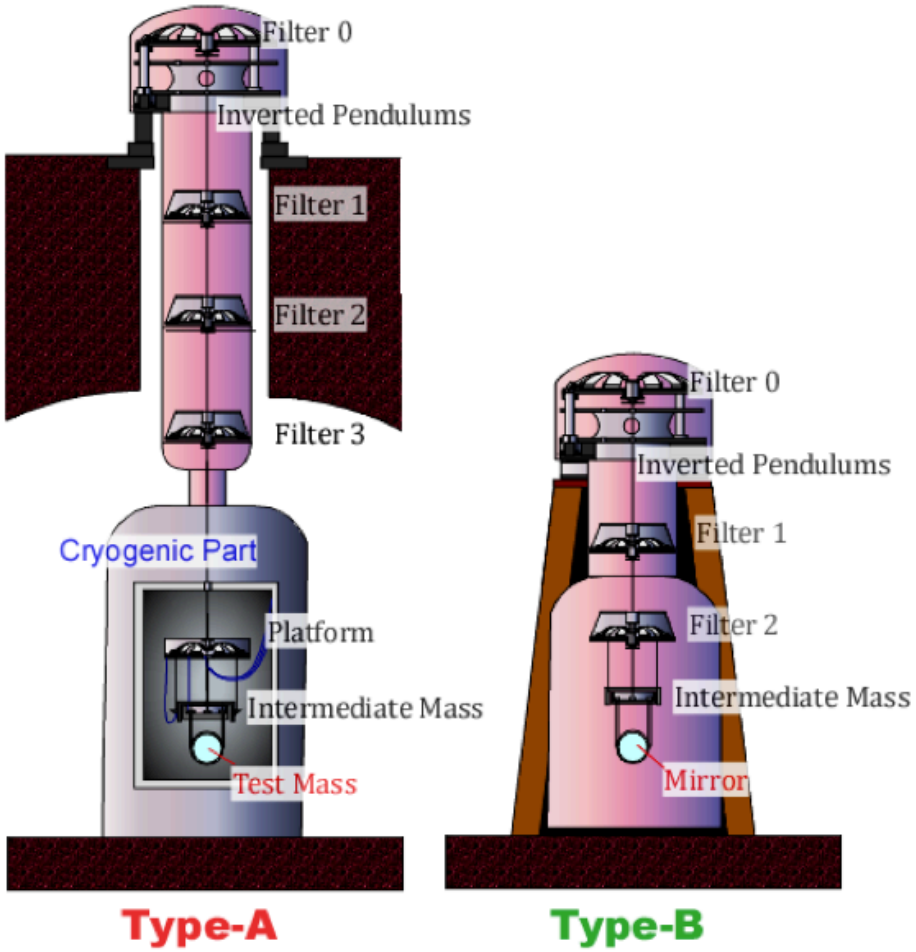

Figure 4: *left: Sketch, not in scale, of Type-A seismic attenuation chain for the cryogenic mirror suspensions. Housed in a 1.2 m diameter shaft containing a 1 m diameter vertical vacuum pipe, it is suspended from an upper tunnel. The overall length of the suspension is 13 m. The cryogenic payload, which is still in the design phase, is shown only for the sake of clarity. Right: Type-B chain for room temperature suspended optics. The top stages of the attenuators are placed on top of a stiff frame anchored to the floor of the main cavern. (The sketches are from [11]).*

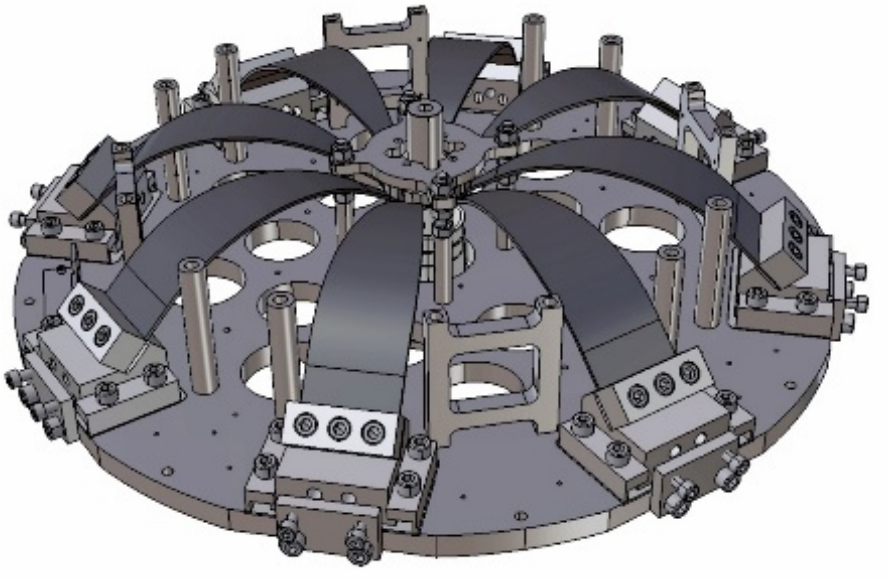

Figure 5: *GAS spring used both in AEI-SAS and EIB-SAS. Eight blades are used to support a 314 kg nominal load.*

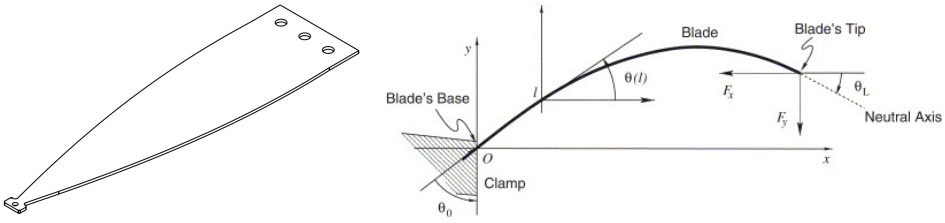

Figure 6: *(left) GAS blade as manufactured. (right) GAS blade two-dimensional model from Cella et al. [17].*

forms a $-33°$ final angle constrained by the geometry of the keystone. The radial position of the clamps is adjusted to realize the required amount of radial/horizontal compression necessary to build up the desired anti-spring effect and lower the vertical natural frequency of the system (see In Fig. 7.)

Both mass and moment of inertia of the blades are not negligible with respect to that of the suspended load and they play a role in the displacement transfer function, causing its saturation to a level, typically, around -60 dB. A compensating device, called *magic wand* [18], can optionally be added to lower the saturation level to -80 dB or even better. In the magic-wand, see Fig. 8, a counterweight is fixed to one end of a rigid tube (silicon carbide is used to push the internal banana mode beyond 250 Hz) while the other end of the tube is connected to the keystone via a thin flexure.

The tube is connected to the filter baseplate via a flexure pivot that allows the counterweight to follow the keystone vertical movement but opposite in phase with respect to the blades. By tuning mass and/or position of the counterweight the effect of the inertia of the blades can be suppressed; almost -90 dB residual transmissibility was demonstrated both at AEI and at Nikhef (see Fig. 9) with the same device.

Inverted pendulum In all mentioned SAS isolators the first horizontal isolation stage is realized by means of an inverted pendulum (IP) platform. The platform is supported by three legs each consisting of a thin walled tube hinged to a stiff base ring by means of a corner filleted circular cross-section flexure providing the elastic restoring force (see Fig. 10 left panel).

Shorter smaller diameter flexures, acting as universal joints, provide the connection between the leg top and the spring box constraining its motion to the horizontal plan. Exception to this configuration is represented by the MultiSAS in which six identical flexures are used in order to raise the natural frequency of the platform bouncing modes. The natural frequency f_0 of the IP is tuned by adjusting the load, exploiting the negative stiffness effect provided by gravity according to:

$$f_0 = \frac{1}{2\pi}\sqrt{\frac{k}{m} - \frac{g}{L}} \tag{1}$$

where k is the lower flexure stiffness, L is the leg length and m is the total IP load (top stage+attenuation chain). Natural frequencies well below 100 mHz can be achieved for an effective passive isolation in the 100-300 mHz region of the microseismic peak. Seismic attenuation performances in the inverted pendulum are limited by the finite inertia of the legs, causing

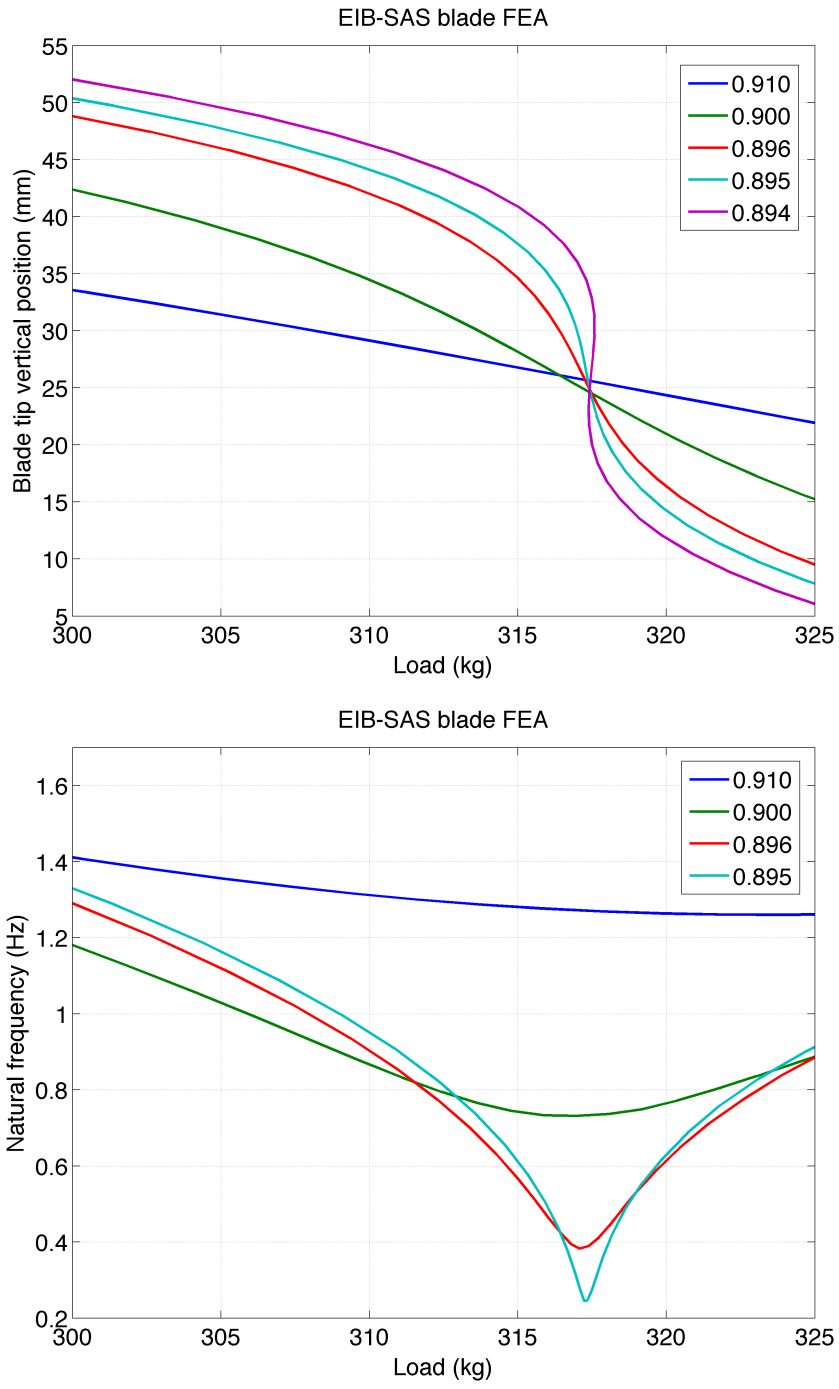

Figure 7: *FEA modeling of the GAS effect on the eight-blades GAS spring designed for EIB-SAS: (top) predicted keystone vertical position vs. load for different radial compression rates. A bistable behavior (purple line), with two different equilibrium position is achieved for compression exceeding a critical value. (bottom) Corresponding vertical natural frequency vs. load.*

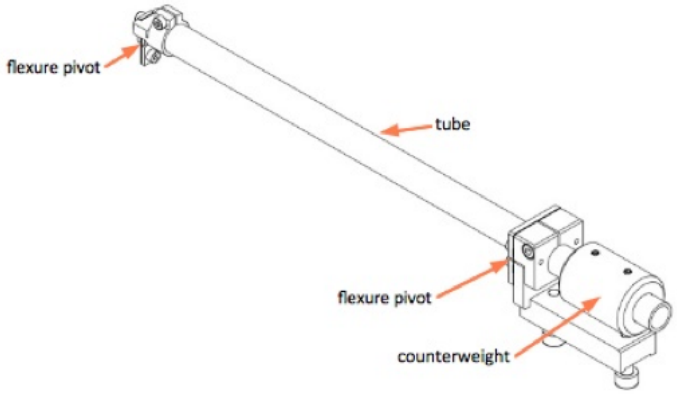

Figure 8: *MultiSAS bottom filter magic wand.*

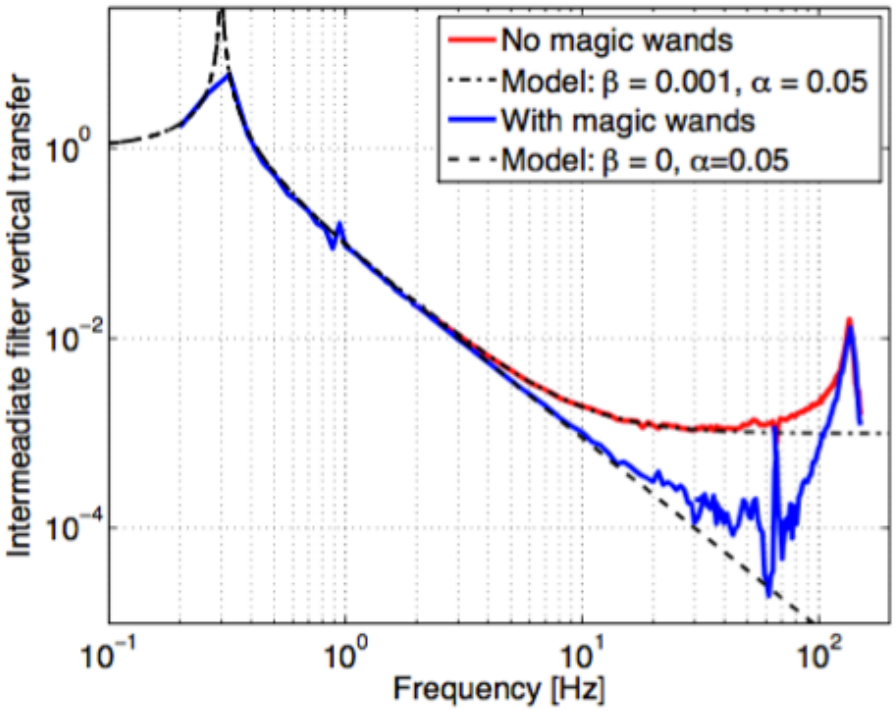

Figure 9: *MultiSAS GAS bottom filter body to payload vertical transfer function. The plot shows the comparison between enabled and disabled (just the counterweights removed) magic wands. The wands, as tuned in the stand alone test, effectively balance the inertia of the blade springs reproducing the* $1/f^2$ *transfer function roll-off characteristic of mass-less springs. The peak at 135 Hz corresponds to the vertical bouncing of the bottom filter keystone on the payload suspension wire.*

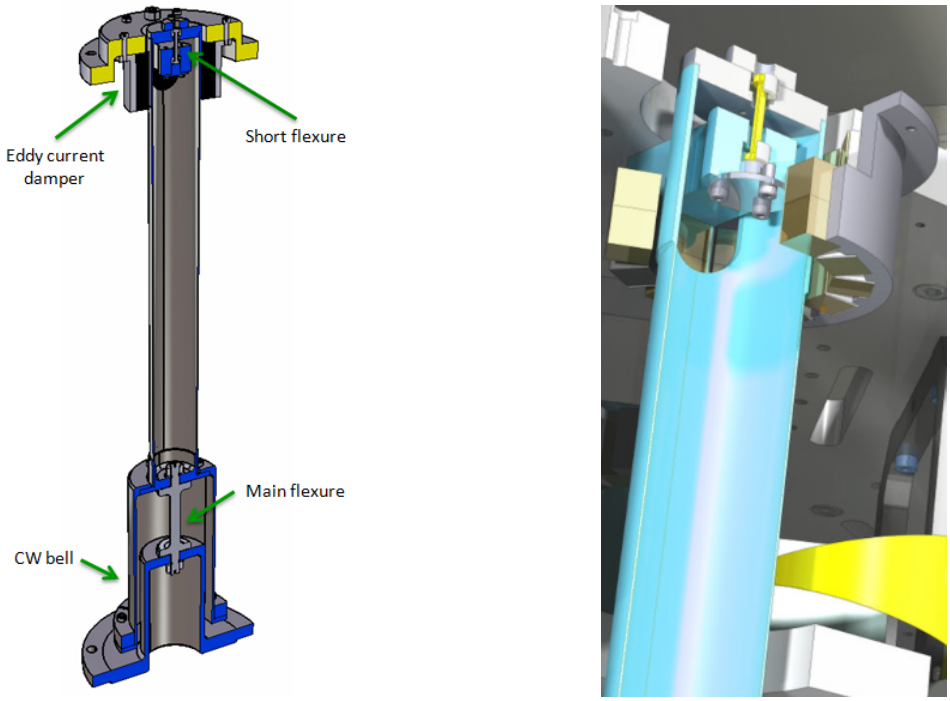

Figure 10: *(left) IP leg cross section. The optional bell to support the counterweights for the compensation of the leg inertia, not implemented in the final configuration, is also shown. (right) Details of the IP leg top. A matrix of permanent magnets, fixed to the spring box bottom plate, faces the IP leg for eddy current damping of the leg internal modes. Because of the vertical position of the magnets, within a few mm from the upper pivot point of the IP, the low frequency eigenmodes are not influenced significantly by the dampers and the horizontal vibration isolation is not spoiled.*

the displacement transfer function to saturate[1], and by their internal modes. In this respect, the short (L=0.5 m) lightweight (leg mass m_l< 1 kg) leg configuration, adopted in all SAS systems after the first implementation in the LIGO HAM-SAS [19], is preferable to the long (around 6-m) leg Virgo design [20]. Transmissibility plateaux of 60 dB are achievable by construction, improvable (see for example the performance of the MultiSAS IP in Fig. 11) by tuning the mass of the counterweight bell so that the center of percussion of the leg is moved as close as possible to the center of rotation of the lower flexure. Internal modes of of SAS IPs are usually well above 100 Hz.

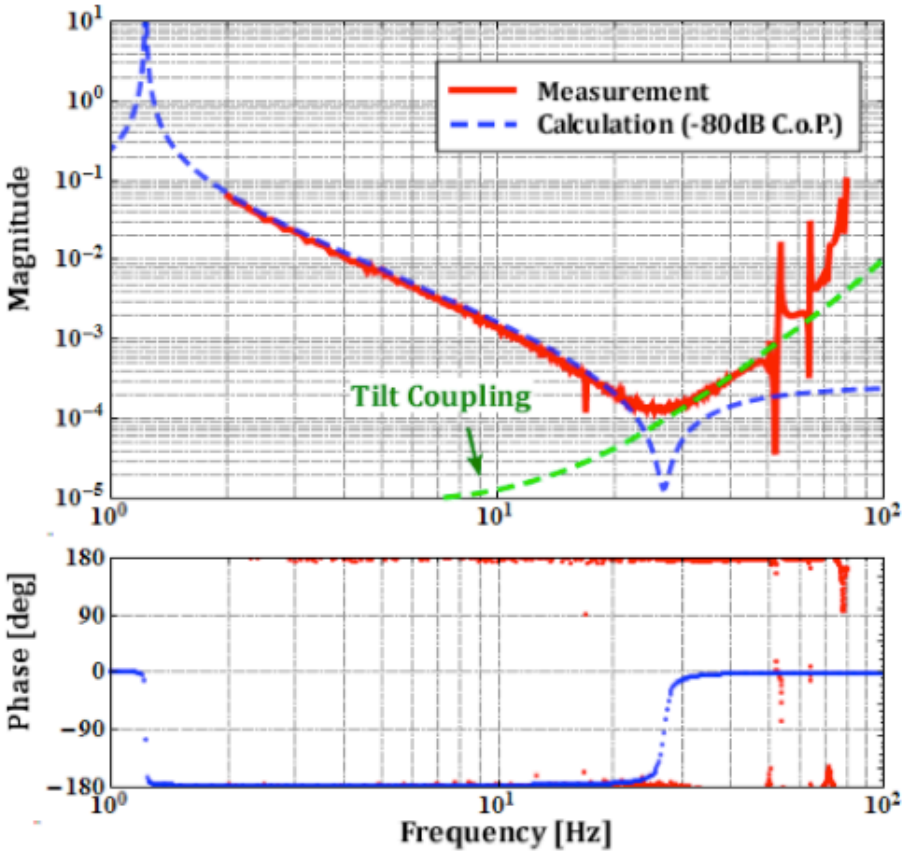

Figure 11: *MultiSAS IP horizontal transfer function measurement. The peak at 1. 3 Hz is due to the recoil of the payload suspension. After tuning of the counterweight mass, the IP response follows the ideal* $1/f^2$ *till about 30 Hz. At higher frequencies the measurement was spoiled by the parasitic pitch motion in the shaking setup.*

A drawback of the short leg IP design is represented by the mechanical qual-

[1]Basic Lagrangian models predict a saturation level around $m_l/6M$, where m_l is the mass of the leg and M is the load per leg. For simple leg shapes, as in MultiSAS, there is a good agreement between Lagrangian and FEA models.

ity factor, lower than in long inverted pendulums since at low frequencies ($\omega_0 \ll \sqrt{g/L}$) $Q \propto \omega_0^2 L/g$, that may make tuning at very low frequencies more challenging. A short IP is also less tolerant than to assembly inaccuracies causing the well known *cradle effect*, i.e. a parasitic tilt of the IP platform when translated; the tilt coupling coefficient, in fact, is inversely proportional to L. Careful engineering and assembly tooling design can largely mitigate such an effect.

The IP platform hosts a low-frequency tuned GAS vertical filter to form the pre–isolator. The KAGRA pre-isolator are virtually identical to the AEI–SAS isolation tables and to the EIB–SAS. AEI–SAS and EIB–SAS (see Fig. 12) systems have three vertical filters supporting optical benches from below, while KAGRA has a single, larger, but otherwise identical filter suspending the isolation chains from above. The same configuration is used in the Multi–SAS isolators (see Fig. 13). Like all mentioned systems, the KAGRA pre-isolator, is directly derived from the successfully prototyped, but never implemented, LIGO HAM–SAS [19].

Besides the pre-isolation function the IP stage, which is tilt rigid, provides an ideal platform for active damping with horizontal inertial sensors (*inertial damping*) of all the modes of the attenuation chain causing any recoil on the stage itself. Thanks to the large dynamic range (about 1 cm in SAS pendulums) the IP is also a valuable tool for horizontal micro positioning of the attenuator payload.

3 Underground environment and seismic suspension

Although it might seem marginal, the definition of the underground environment, devoted to host a mechanical attenuator designed to isolate from seismic disturbance the payloads, is a crucial preliminary step leading to a clear description of the main characteristics of the suspension system.

3.1 Tilt of the tunnel hosting the interferometer

By far the most daunting feature of KAGRA's site is the 0.3 % inclination of its tunnels. Vertical springs have orders of magnitude more dissipation than horizontal pendulums, and more thermal noise. Because of the inclined beams, 0.3 % of the vertical thermal noise of the lowest spring will couple directly into the interferometer noise budget, unless we find a way to filter it out by an extremely low-loss vertical compliance. The vertical spring thermal noise contribution can easily dominate over the thermal noise of

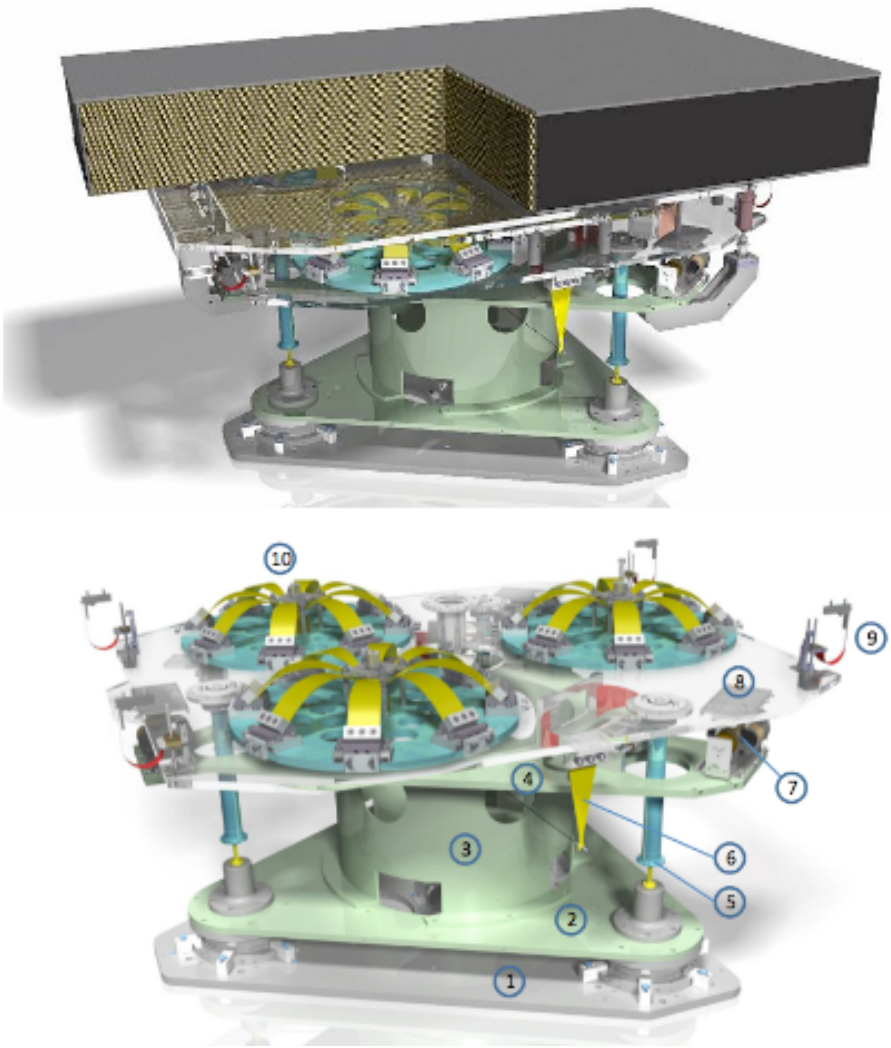

Figure 12: *Top: impression of the Advanced Virgo External Injection Bench as supported by the EIB–SAS single stage vibration isolator. Bottom: EIB–SAS view. 1.Ground plate; 2. Inverted pendulum baseplate; 3. Sensor platform support; 4.Sensor platform; 5. Inverted pendulum; 6.Tilt stiffener; 7. Horizontal LVDT/actuator; 8. Spring-box bottom plate; 9. Vertical correction spring; 10.GAS filter.*

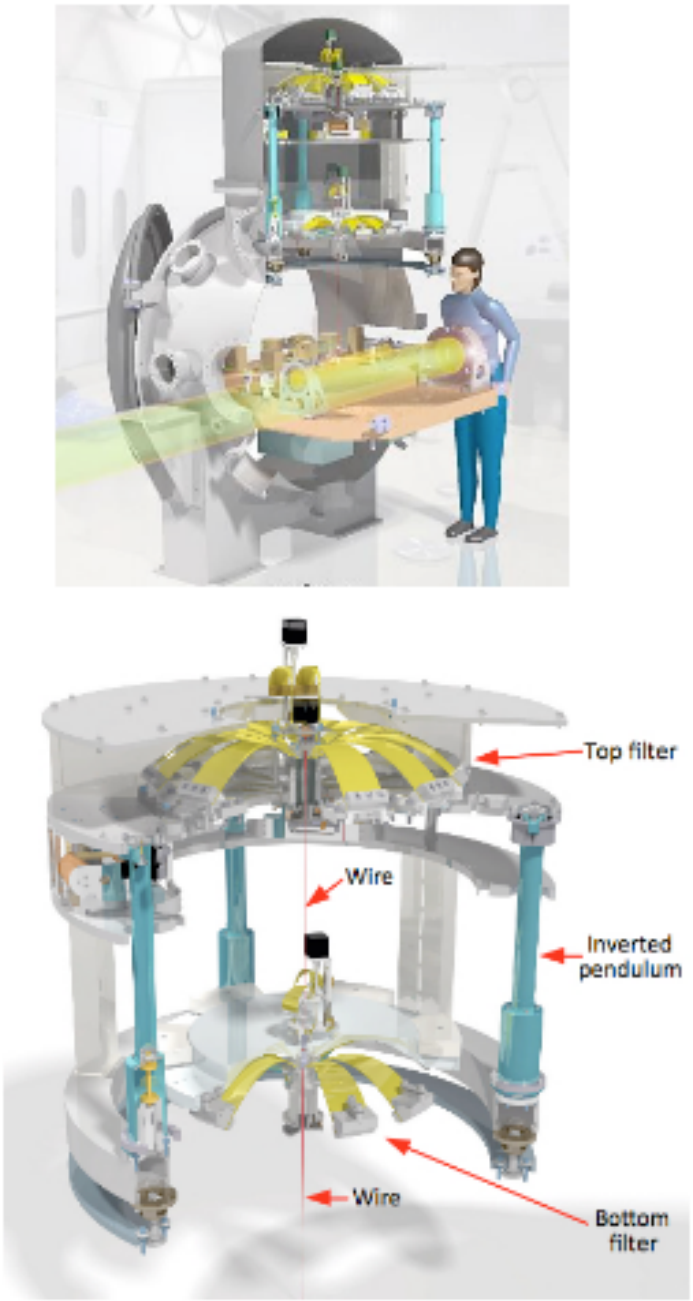

Figure 13: *Top: impression of the Advanced Virgo End Bench as supported by the MultiSAS multistage seismic attenuator. Bottom: MultiSAS overview.*

the pendulum mode. Failure of properly addressing this problem will completely negate all advantages of cryogenic suspensions. The inclined tunnel is a peculiar characteristic of KAGRA, imposed only by local rules related to the presence of heavy–metal–contaminated water in the Kamioka mountain. Tunnels, even longer ones like the tunnel under the British channel, are routinely made horizontal elsewhere. However, Earth's is not flat, and a horizontal tunnel follows Earth's surface curvature, while light beams travel in straight line. Therefore, even splitting the difference, i.e. accepting the opposite deviation from verticality at both ends, Earth's curvature imposes a deviation from verticality of about 10^{-4} per km at the end of a long beam–line. Therefore in a detector with 10 km long arms like ET, the end stations will unavoidably be tilted away from horizontality by about 10^{-4} radians, which is about 1/3 of KAGRA's slope. To mitigate the vertical thermal noise problem, KAGRA's final mirror suspension stage must include low-mechanical-dissipation vertical springs, an engineering requirement which is much more difficult to satisfy than building the cryogenic suspension wires. KAGRA is subject to about ten times more slope than if it was horizontal. Therefore it needs ten times more suppression of vertical thermal noise, which means it requires ten times softer final suspension springs. Any solution devised to mitigate the vertical noise percolation into the KAGRA interferometer will be directly applicable to the suspensions of third generation gravitational wave detectors. On the other hand, third generation observatories will aim to Gravitational Wave detection at ten times lower frequency, therefore requiring low-noise springs operating at one order of magnitude lower frequency. This means these new detectors will need another factor of ten softer springs than in KAGRA. This is an extraordinarily stringent requirement, which most likely will be a limiting factor. It is vital, to minimize the problem, that third generation interferometers be designed with horizontal tunnels.

3.2 Technical noise sources

In present observatories the majority of the mechanical noise introduced by human activities is due by the instrumentation operation noise of the electronics, air conditioning, pumping and other facility noises. Yet in an external building the instrumentation noise can radiate freely and dissipate rapidly. In a tunnel all this noise is bottled-in and reverberates with likely noise amplification effects. It is a serious problem; the pulse–tube cryocooler noise is of particular concern. Electrical power line noise is also a concern, as substantial power is consumed in close confines. In a tunnel a vigorous air flow must be continuously maintained to remove rock heat, waste heat from instrumentation and machinery possible gas exhalations from the rock, and to renew air. Air flow is a known generator of acoustic noise in tunnels.

Besides white noise, often organ pipe resonances are excited. In addition tunnels, especially straight ones, act as sound–guides, carrying machinery's noise over very long distance, and buffering with walls and doors is often limited by the necessity of maintaining the air flow. Finally the vacuum works couple very effectively with any channeled acoustic noise.

3.3 Tunnel design

The solution devised to mitigate the above mentioned problems in KAGRA is the double tunnel configuration illustrated in Fig. 14 [21]. The head of the isolator chain is solidly footed on the rock floor of a short auxiliary tunnel, crossing the main tunnel at a higher level, directly above the interferometer test mass locations.

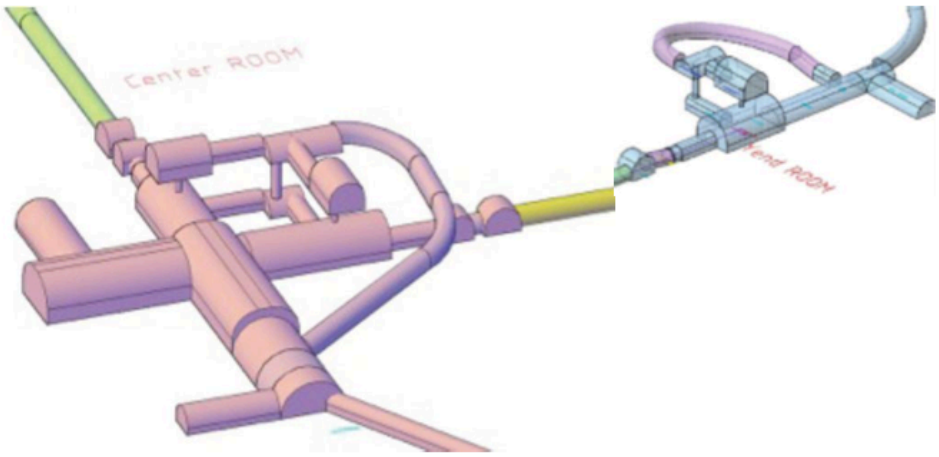

Figure 14: *Structure of the KAGRA tunnels around the beam splitter (left) and one of the End Test Masses (right). The inclined ramps connect the main tunnel level with the auxiliary rooms housing the head of the type–A attenuation chains, 13 m higher.*

The auxiliary tunnels are much quieter than the main tunnel because they are dead-end tunnels, accessible through a twisting ramp that can be closed off with doors. The attenuation chain hangs down through a small–diameter vertical well connecting the two tunnels. The vacuum pipe housing the attenuation chain also hangs down in the well from the top tunnel, it is connected to the top flange of the cryostat in the lower tunnel through a bellow that decouple mechanical vibrations. The empty space between the vacuum pipe and the well walls is buffered with light foam to keep the well from acting as sound guides. The footings of the attenuation chains are further decoupled from any possible vacuum tank vibration by bellows. This solution

effectively mitigates any vibration of the cryogenic pumps, instrumentation and ventilation because the suspension are completely separated from the vacuum tube and all connections to ground are to the solid rock floor of a physically separated tunnel. Such a layout, with a short and rigid connection of the seismic isolators to the bedrock, also minimizes problems related to the compliance of intermediate support structures experienced in both LIGO and Virgo. Safety concerns, encountered while building and maintaining the Virgo superattenuators because of their height, are also eliminated. Working on such tall structures entails serious danger of falling or dropping tools, and required the addition of large scaffolding that encumber the space around the superattenuators, and can induce extra mechanical noise. Finally, the double tunnel solution has three additional advantages, briefly described as follows.

1. The required size of the halls housing the test masses is reduced by the double tunnel solution, therefore allowing reduction of the maximum transversal size of the hall and of the amount of excavation. Smaller excavation sizes reduce the surface stress on the rock and the required strength of the excavation's lining. Having introduced less disturbances to the rock, one can expect a more stable hall, less prone to rock creep and/or cracking. The stability advantage also reflects on the excavation's cost. The cost of an excavation grows faster than the cube of its smallest dimension. In KAGRA's relatively small halls the cost of the two tunnels plus the cost of the access ramps were roughly equal to the cost of the larger cavern initially foreseen. Large cost advantages are expected for the case of third generation detector xylophones, which will require substantially larger spaces.

2. Separating the two tunnels by a larger distance, the length of suspension wire between attenuation filters can be made arbitrarily long. Longer wires lead to lower pendulum resonant frequency, a requirement for lower frequency gravitational wave detectors. KAGRA did not directly use this advantage because the 5 m minimal separation between tunnels dictated by the local rock strength already lead to suspension wires longer than necessary. Having available more height than strictly necessary was useful in KAGRA, to implement a modified filter immediately below the attenuation chain head, whose main function is to damp the chain's internal modes and make lock acquisition easier. Given Virgo experience, the chosen configuration will assuredly deliver the attenuation required by KAGRA with a large safety factor. The low frequency detector of ET's xylophone will require longer wires between filters. Wires of arbitrary length can be trivially implemented by increasing the separation between the upper and lower tunnel, and of the connecting well. Parallel tunnels closer than one diameter are unstable. Therefore to minimize the vertical

separation the upper tunnel was excavated at 90 degrees with respect to the main tunnel. (lower tunnel 12 m, upper tunnel 8 m, separation 5 m, see Fig. **??** and Fig. 14). As soon as the vertical separation exceeds the tunnel diameters, parallel tunnels can be excavated. This will be useful in third generation gravitational wave facilities where each tunnel will house multiple beams, each with Fabry-Perot mirrors at different locations along the tunnel. In KAGRA, due to the short length required (5 m) the seismic isolation wells were simply blasted with dynamite. The much longer wells needed for third generation gravitational wave detectors can be cheaply and safely excavated in hard rock with the raise boring technique.

3. The attenuation chain can be easily and safely installed by lowering it in the well from the top tunnel. An important consideration in designing smaller size vacuum chambers is that also smaller diameter access tunnels or wells will be allowable and tunnel like experimental halls becomes feasible. This is not a negligible cost; because of safety considerations each experimental hall will need its own access. In a fixed budget scenario, smaller volume excavation for access and experimental halls can be traded for longer tunnels, which directly increase the observatory sensitivity to gravitational waves.

In addition, if tunnel-like experimental halls with same, or only slightly larger, diameter than the long tunnels can be used, deeper facilities become feasible practically at no extra cost. While Raleigh waves and other perturbations radiating from the surface becomes only slowly weaker with depth even a small gain in low frequency sensitivity due to lower Newtonian noise translates immediately in increasing by a corresponding the highest mass of detectable black holes, a non negligible astrophysics advantage.

4 Type-B Seismic Attenuation System

The isolation chain topology, introduced in Fig. 4, is illustrated with more details in Fig. 15. The expected performances, resulted from 3D rigid body simulations are shown in Fig. **??**

Each component of the attenuation chain has specific functions, in certain cases hierarchically overlapping. We remind that the mirror actuator authority must be minimized because their force noise is proportional to the electronics noise, and large control authority would produce control noise overwhelming the gravitational wave signal. Besides attenuating mechanical noise in the gravitational wave detection band, the most important function of the chain is to reduce the low frequency r.m.s. motion of the mirror well below the range that can be handled within the authority of the mirror con-

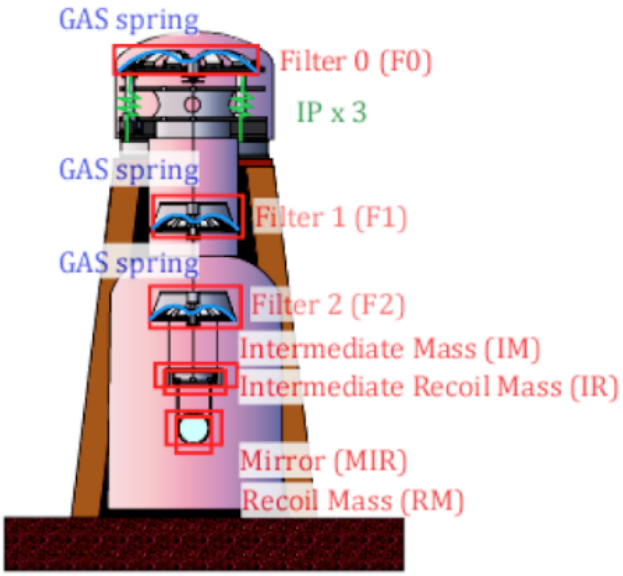

Figure 15: *Block scheme of Type-B seismic isolators.*

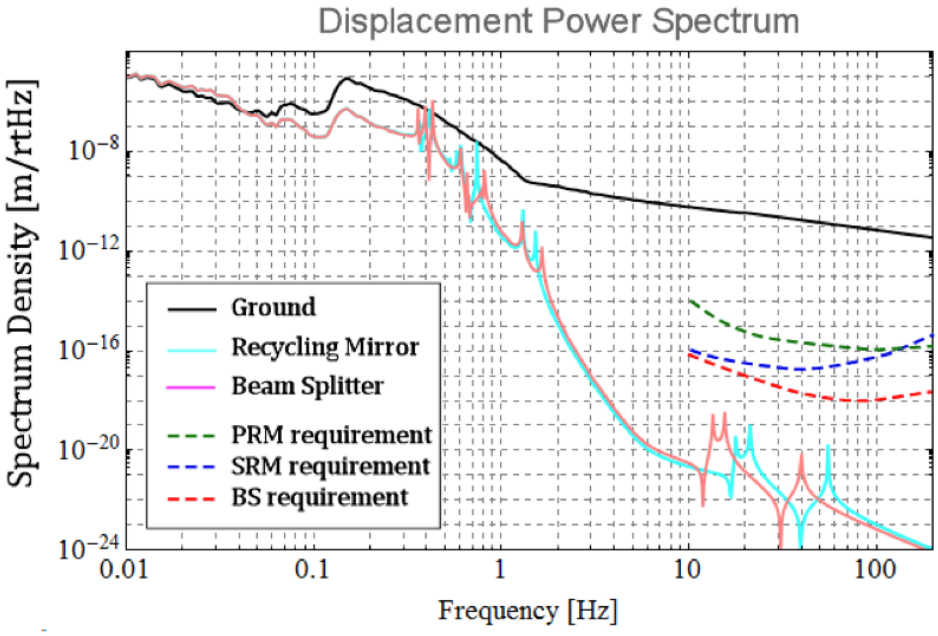

Figure 16: *Estimation of the mirror displacement induced by seismic vibration in the type-B system from [11].*

trol actuators. This second function is shared by several components along the chain. The pre–isolator has the following functions:

1. Provide sufficient low frequency isolation at the micro-seismic frequency level to reduce the r.m.s. motion of the mirror in that frequency range.
2. Actively or passively damp any attenuation chain resonance that could be excited with amplitude exceeding the mirror control authority.
3. Micro-position the attenuation chain head and the mirror in the longitudinal, transversal, vertical and in yaw degrees of freedom.
4. Provide a share of seismic the attenuation in the interferometer GW detection band (above 10 Hz).
5. Provide a diagnostic and calibration tool to ensure the performance of the rest of the chain.

The standard filters are designed to provide the bulk of the attenuation in the GW detection frequency band. The vertical attenuation is obtained through cantilever springs and the horizontal attenuation as a chain of simple pendulums. The eddy current damping ring is primarily designed to damp the yaw motion of the attenuation chain. It is a key element to reduce the yaw r.m.s. motion and therefore the authority demanded on the mirror actuators. As an added benefit it damps also the violin modes of the attenuation chain, and to some level its pendulum mode. It thus reduces the r.m.s. motion of the mirror in the intermediate frequency range (from a fraction to a few Hz).

Filter 2, so-called *bottom filter* has the additional functions of providing:

1. independent suspension of the intermediate mass and the intermediate-mass recoil mass
2. fine pitch, yaw and vertical relative positioning of the intermediate mass recoil mass with respect to the intermediate mass.

The intermediate mass functions are to provide:

1. independent suspension of the mirror and the mirror recoil mass
2. static pitch positioning of the mirror

The intermediate-mass recoil-mass functions are:

1. to carry the dynamic actuators and position sensor acting on the intermediate mass
2. to provide dynamic control forces on the intermediate mass in all six degrees of freedom by means of strong collocated sensor/actuator pair s

(OSEM [22]) to reduce the control authority required from the mirror position actuators below the limits imposed by their required noise level.

The mirror recoil mass functions are:

1. to carry the dynamic actuators and position sensor acting on the mirror
2. to provide dynamic interferometer lock control forces on the intermediate mass in the longitudinal, pitch and yaw degrees of freedom by means of low-force, low-noise OSEMs.

The static positioning in all five degrees of freedom (excluding mirror roll) are designed with remotely controlled mechanical settings to be only occasionally changed to allow all dynamic actuators to work around a null static force.

4.1 The inverted pendulum stage

4.1.1 Mechanics

The horizontal attenuation of the KAGRA pre–isolator, is provided by an inverted pendulum table composed by three legs, each consisting of a 1-mm walled, 440 mm long, 48 mm outer diameter, 180 g mass aluminum tube, distributed on a 1236 mm diameter circle. The legs support a 1340 mm diameter steel disk forming the table and the base of the vertical pre-isolator GAS filter. The mass of the pre-isolator filter is more than 300 kg. The natural frequency will be tuned to 30-50 mHz to provide attenuation at the microseismic peak, while 80 dB asymptotic vibration isolation, typical for SAS systems, is expected to be achieved after tuning of the leg counterweights. Internal resonances (around 100 Hz) of the legs are very effectively damped by eddy current dampers mounted around the leg's head.

4.1.2 Controls: sensors and actuators

Position control The inverted pendulum base structure needs to be precisely leveled. It is supported on three points by means of through–vacuum supports. These through-vacuum supports are mechanically separated from the vacuum tank by bellows, so that the vacuum tank vibrations are not transmitted to the attenuation chains. These three supports sit on precision hydraulic pistons that allow leveling of the inverted pendulum base structure parallel to the effective inverted pendulum horizon within a few parts per million. The effective horizon felt by the inverted pendulum is the setting at which the table sits centered with respect to its base, and it may differ

from the actual horizon because of small machining and assembly errors on the base and the flexures. Provision is made to offload the pressure from the cylinders after leveling is completed. The residual transversal (X and Y) and angular (yaw) static adjustments of the inverted pendulum working point are applied by three stepper motor controlled tuning springs placed at 120° on the outer diameter of the inverted pendulum table. Their design (see Fig. 17) is the same as in AEI-SAS, EIB-SAS and MultiSAS.

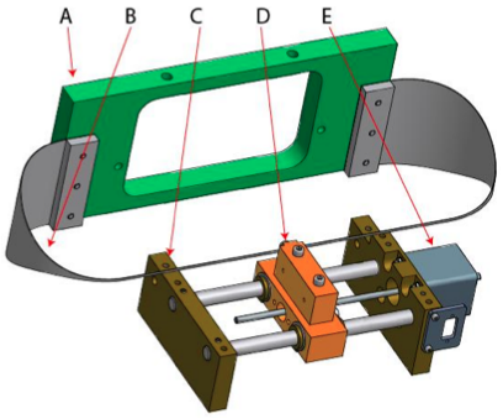

Figure 17: *Stepper motor controlled springs for Inverted pendulum static positioning. A: Spring holder, on moving table, B: Blade springs, C: Stepper motor support and slider guide, on base structure, D: Slider, E: stepper motor with long threaded shaft.*

The position of the inverted pendulum table is monitored by three LVDT sensors [23], placed opposite to the static springs. These LVDTs, shown in figure Horizontal LVDT and Voice Coil Actuator, have nanometer resolution and several mm range. Dynamic control of the inverted pendulum table and tidal working point corrections are applied via constant force voice coil actuators [24] (5 N/A) collocated with the LVDT shown in Fig. 18.

Inertial damping Space is foreseen on the KAGRA's inverted pendulum table for implementation of uniaxial accelerometers [25] or geophones for active seismic attenuation and inertial damping of the chain collective modes. Simulation of the inverted pendulum control are discussed in the dedicated section of this document.

4.2 Vertical pre–isolation filter

The low frequency vertical pre-isolation is provided by a large GAS filter, also known as top filter. The pre-isolator filters in the type–A and type–B

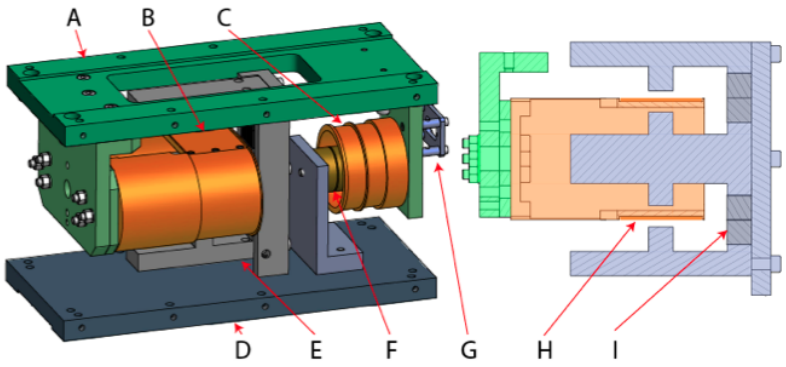

Figure 18: *Horizontal LVDT and Voice Coil Actuator. Green and Orange: moving parts; gray and blue: static parts. A: Moving sensor-actuator plate, B: Actuator racetrack coil support, C: LVDT secondary support, D: Static sensor-actuator plate, E: Magnet Yoke, F: LVDT primary, G: cable connector, H Actuator winding, I actuator permanent magnets.*

chains differ only on the number and width of their suspension blades, 6 blades for the four type-A filters and 3 blades for the seven type-B. The top filter fulfills several functions besides providing low frequency vertical attenuation:

- Static micro-positions the attenuation chain in the vertical direction
- Sensing of the vertical working point and motion of the chain
- Static micro-positions the attenuation chain in the yaw DOF
- Vertical dynamic actuation of the attenuation chain
- Provide a inertial vertical sensor platform for active attenuation
- Support the eddy current damper for the first standard filter.

4.2.1 Blade design

All KAGRA–SAS blades, both for top and standard filters, have the same profile function as blades in AEI-SAS and EIB-SAS GAS springs. The width along the blade length $w(\xi)$ is given in polynomial form by:

$$w(\xi) = w_0 \cdot (1 + 0.177\xi - 1.109\xi^2 - 0.455\xi^3 + 0.51\xi^4) \qquad (2)$$

where $\xi = x/L$ is the adimensional coordinate along the blade length and w_0 is width of the blade at its base. Blades for standard filters are identical

to EIB-SAS ones (w_0=80 mm, L=274 mm, thickness t=2.4 mm), while the top filter blades (w_0=125 mm, L=606 mm, t=5 mm) were just resized for a larger loading capability using the scaling law:

$$\frac{M_2}{M_1} = \frac{w_2 L_1^2 t_2^3}{w_1 L_2^2 t_1^3} \tag{3}$$

where M_2 and $M1$ indicate new and initial load at the working point. The ratio t/L has been kept constant to maintain the same stress level. Stress profile for EIB-SAS like blades have been extensively investigated by both FEM modeling and experimental characterization [26]. FEM model of the blade at the working point is shown in Fig. 19. Due to effect of the Poisson ratio the stress distribution differs between top and bottom surface. Stress concentration at the edges of the blades is predicted and validated by measurements. The model predicts a von Mises stress peak value of 1.8 GPa to be compared with the 1.92 GPa ultimate tensile strength of maraging C250. Measurements of the radius of curvature of the blades in an assembled GAS filters have shown a slightly larger safety margin (few percent lower stress than in the FEM model).

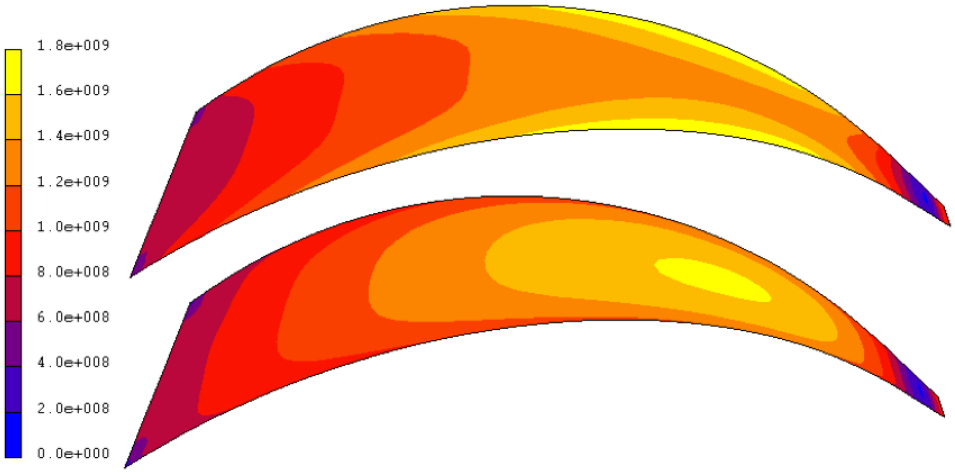

Figure 19: *Stress in the top (upper) and bottom (lower) surface of the KAGRA-SAS GAS filter blades according to the FEM analysis for a Poisson ratio ν = 0.32. Due to corrugation of the blade the stress in reduced in the middle of the top surface and along the rim of the bottom surface. The stress is enhanced along the rim of the top surface and in the middle of the bottom surface. The maximum stress is 1.80 GPa in the top surface and 1.62 GPa in the bottom surface.*

4.2.2 Controls

The pre–isolator GAS filters are provided with a stepper-motor-controlled parasitic vertical spring illustrated in Fig. 20 that is used to adjust the height of the mirror. This movement is done at the price of moving the filter slightly off its best working point, a down side that can be corrected with a suitably profiled electromagnetic spring.

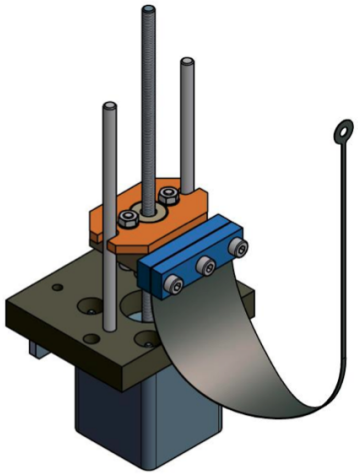

Figure 20: *Stepper-motor-controlled parasitic vertical blade, for working point tuning of the pre-isolator filter. The motor is attached to the filter base plate, the tip of the spring to the keystone. The blade is flat at production. The blade's profile is calculated to give it circular bending around when under tension. The design is the same as in AEI-SAS and EIB-SAS adjustment springs.*

In addition the pre-isolator filter is provided with a rotation mechanism that align the yaw of the mirror to the beam axis. In the mechanism, the suspension wire head holder rests on a ceramic ball thrust bearing, and rotation is achieved by means of a stepper motor pushing on a lever arm.

Dynamic control on the vertical attenuation chain is done by means of an LVDT (± 5 mm linear range and 1 nm/$\sqrt{\text{Hz}}$ self noise), measuring the position of the keystone with respect to the filter plate, and a collocated voice coil actuator (15 N/A) (see Fig. 21 [13]). The pre–isolator filter keystone is also provided with a support structure for an optional vertical inertial sensor.

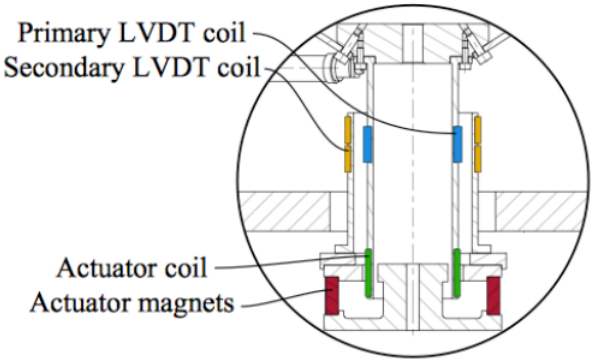

Figure 21: *Schematic view of the collocated LVDT/voice-coil actuator installed on each GAS filter. Such a configuration was introduced for the first time in TAMA-SAS and since then reproduced in all built SAS systems.*

4.2.3 Low frequency tuning limitations

The vertical pre–isolator is instrumented with two magic wands and therefore, after their tuning, its transmissibility is expected to saturate around 80–90 dB as in MultiSAS filtering stages. On the low frequency side the pre–isolator is intended to passively attenuate the micro–seismic noise peak between 100 and 300 mHz. While it is theoretically possible to set the radial compression for very low resonant frequencies, limitations are encountered in reality due to physics of the GAS principle itself and due to material inelasticity. Despite the blades are built with maraging steel, one of the strongest, creep-free and most elastic (low loss) metal available, the elastic constant cancellation of the GAS configuration turns into very low mechanical quality factors and exposes even tiny deviations from elasticity of the material [27]. It has been observed [28] that, at low frequency tuning, GAS springs shows strong *hysteresis* and that metastable equilibrium points exist around the mathematical equilibrium position. In such a regime, governed by the dislocation's collective activity (stochastic entanglement and avalanches) inside the material, instabilities may also occur triggered by temperature oscillations, as well as by other perturbations. This makes it practically impossible, in an open laboratory, to stably tune a GAS filter much below 100 mHz for a large pre-isolator filter and much below 200 mHz for a standard filter. More aggressive low-frequency tuning may be useful for possible low-frequency upgrades of KAGRA, but it will be a necessity for future gravitational wave detectors, sensitive to lower frequencies. Lower frequency tunes are possible when operating filters in vacuum, with tight temperature control and positive feedback strategies (so called *Electromagnetic anti-spring* [29]). A pilot in vacuum test of the HAM-SAS demonstrated operation of standard filters close to 10 mHz vertical frequency for several hours [19]. More tests will be

necessary to establish a suitable procedure and the reliability of these tunings. A better solution would be to use elastic materials free of dislocations, and therefore free of instabilities; no such material is identified, at present, although some bulk glassy metals are good candidates.

4.2.4 Prototype test

A full scale vertical pre-isolator for Type–B chains was built and characterized. Natural frequency at the working point (steepest point in the keystone vertical position vs. load curve) was measured as a function of the radial compression (see Fig. 22). The square–root function observed behavior supports the picture of an introduced negative stiffness proportional to the compression rate. Fig. 23 shows the final filter working point tuning: at a specific compression rate the natural frequency is measured as a function of the vertical position of the keystone.

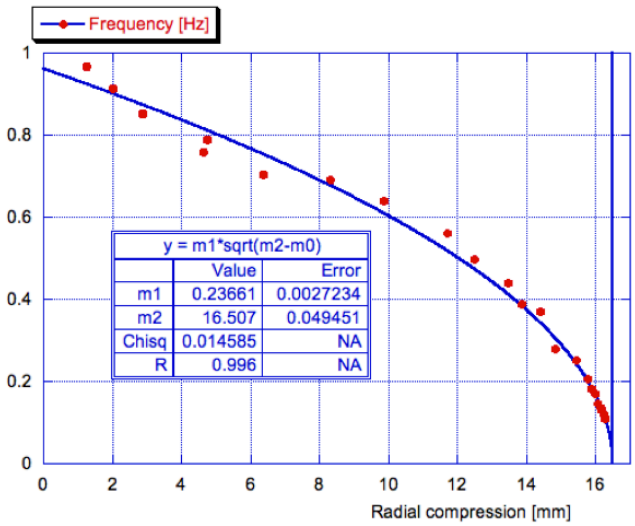

Figure 22: *Resonant frequency at the working point versus radial compression of a pre-isolator filter. The radial compression is conventionally measured as the distance in mm between the back surfaces of the blade base clamp and the back of the two clamps that hold it onto the top surface of filter's base disk.*

Fig. 24 shows the mechanical quality factor measured at different natural frequencies. The observed frequency dependence turns out to be well described assuming the internal friction of the material to be dominated by thermoelastic damping (see next paragraph for details).

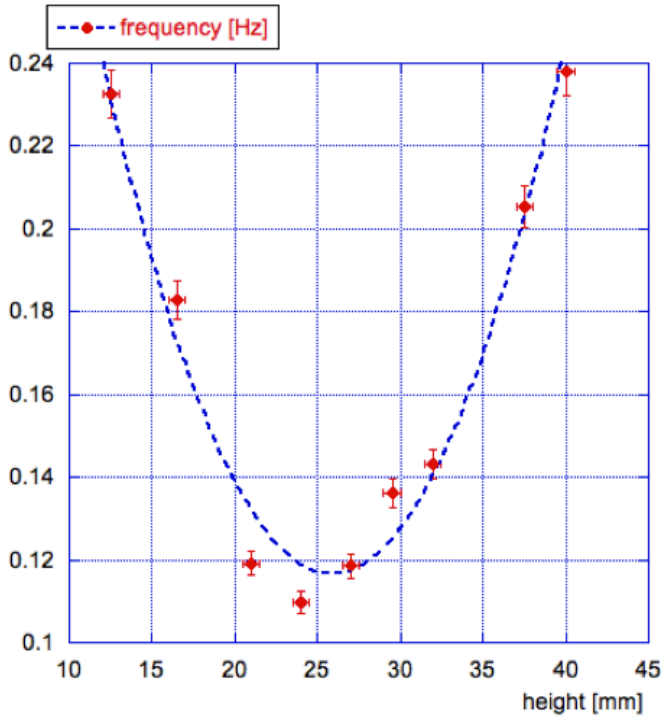

Figure 23: *Search of the Filter working point. The different heights are obtained by adding or removing small masses, typically one or few 100 g.*

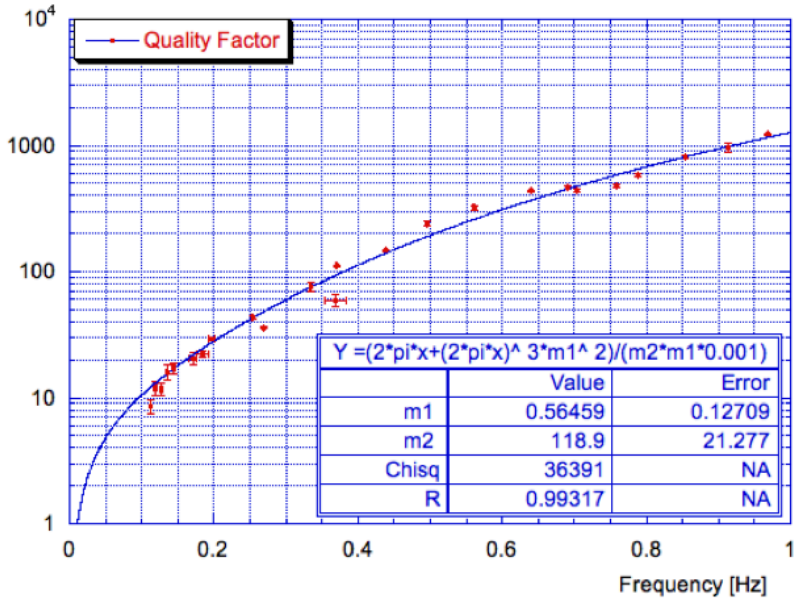

Figure 24: *Quality factor versus frequency in a pre-attenuator filter.*

E (GPa)	α (ppm $\cdot$ °K^{-1})	C_v (J $\cdot$ m^{-3} $\cdot$ °K^{-1})	κ (W $\cdot$ m^{-1}°K^{-1})
186	11	$6.5{\cdot}10^6$	25.5

Table 1: Thermo–mechanical properties of maraging steel C–250 at 300 °K.

Thermoelastic damping model Internal damping in mechanical oscillators is generally modeled by introducing a complex stiffness in the Hooke's law:

$$F = -k(1 + i\phi(\omega))x. \tag{4}$$

In time domain, if the force F is sinusoidal, $\phi(\omega)$ represents a delay between F and the displacement of the oscillator mass. It's easy to verify that $\langle \frac{\partial E}{\partial t} \rangle$, the time average of the dissipated power, is proportional to ϕ (as long as $\phi \ll 1$); more specifically a fraction $2\pi\phi$ of the energy stored in the oscillator is dissipated in each cycle of oscillation. Major cause of energy dissipation in spring elements under dynamic stress, is the *internal friction*, related to irreversible deformation of crystals in the core material and generally associated with the dynamics of dislocations. The loss angle related to internal friction ϕ_{int} is typically frequency independent and for maraging steel literature reports $\phi_{int} = 10^{-4} \div 10^{-5}$. Systematic effects like stick–and–slip losses localized at the spring element clamping points or excess losses localized on the surface may add on top of ϕ_{int} with the same frequency independency characteristic. Another important source of dissipation in springs is *thermoelastic damping*, which arises from the coupling of temperature with the strain because of the nonzero thermal expansion coefficients of materials. When a flexure is bent one side heats and the other cools, and then heat flows thru attempting to restore equilibrium. The theory of this mechanism was given by Zener. According to the model the corresponding loss angle ϕ_{ted} is given by:

$$\phi_{ted}(\omega) = \Delta \cdot \frac{\omega\tau}{1 + \omega^2\tau^2} \tag{5}$$

where

$$\Delta = \frac{E\alpha^2 T}{C_v} \tag{6}$$

with E the Young modulus, α the thermal expansion coefficient, T the temperature and C_v the specific heat per unit volume (see values at 300 °K in Table 1). At room temperature Δ=0.001.

The characteristic frequency $f_0 = 1/2\pi\tau$ for a thin plate is:

$$f_0 = \frac{\pi}{2}\frac{\kappa}{C_v t^2} \tag{7}$$

where κ is the thermal conductivity and t is the thickness of the plate. For a blade 4.9–mm thick (as in KAGRA top filter) f_0=0.26 Hz. The Zener model predicts peak losses around f_0 while the effect is depressed both for $\omega\tau \ll 1$ and $\omega\tau \gg 1$. Intuitively this behavior can be explained considering that at low frequencies the strain field changes very slowly compared to the thermal response of the material and then the exchange of energy with the thermal bath is basically adiabatic and reversible. On the other side, at high frequencies, the thermal response is too slow and no heat flow develops. In Fig. 25 is shown the thermoelastic loss angle predicted for different blade thicknesses.

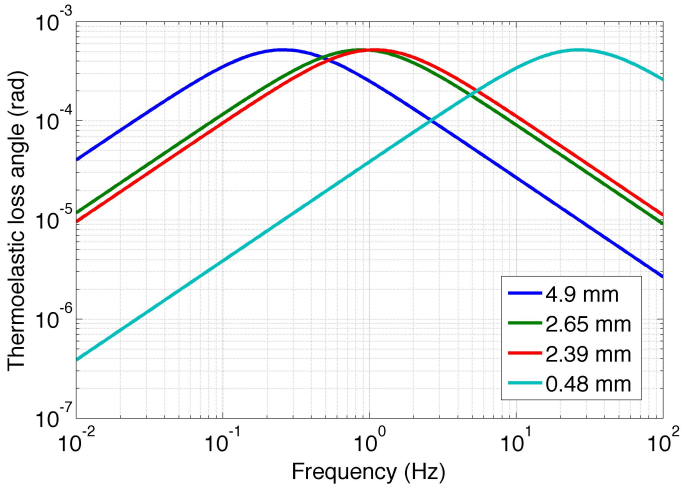

Figure 25: *Thermoelastic loss angle calculated for some reference GAS blades: the 0.48–mm thick from Mini–GAS, the 2.39–mm from EIB–SAS, the 2.65–mm from the MultiSAS top filter and the 4.9–mm one from the KAGRA top filter.*

In general the various contributions to the loss angle just add up as:

$$\phi = \phi_{int} + \phi_{ted} + \phi_{clamp} + \phi_{surf} + ... \tag{8}$$

In the case of a mass supported by a simple cantilever blade (in the sense that the blade is just bent, no axial load is present), and in absence of viscous damping forces, the mechanical quality factor Q is just $Q = \phi^{-1}$. In GAS filters low effective stiffness k_{eff} is achieved by finely balancing much larger positive k_{pos} and negative k_{neg} stiffness contributions

$$k_{eff} = k_{pos} - k_{neg}. \tag{9}$$

Around the working point a very small change in k_{pos} and k_{neg} causes dramatic changes in k_{eff}. When the GAS filter oscillates, both spring and anti–spring consume energy each proportionally to the respective stiffness and imposed deflection, according to Equation 1. While by tuning the natural frequency ω doesn't change in a relevant way the amount of energy dissipated per cycle of oscillation (unless ϕ has some frequency dependence), on the other side the energy available for the oscillation is proportional to k_{eff} and then it changes as ω^2. Therefore in analogy with the inverted pendulum the quality factor is expected to be something like:

$$Q = \frac{1}{\phi(\omega)} \cdot \frac{\omega^2}{\omega_e^2} \tag{10}$$

where ω_e is the asymptotic value to which ω converges at null blade lateral compression. If we consider just thermoelastic damping (as it is expected from Fig 1) then the quality factor is:

$$Q_{ted} = \frac{\omega + \omega^3 \tau^2}{\omega_e^2 \tau \Delta} \tag{11}$$

The experimental points from the KAGRA top filter prototype fit well (see Fig. 24) with the model of Equation 8. From the fit we get f_0=0.27 Hz, which is in remarkable agreement with the theory, and $f_e = \omega_e/2\pi$=1.7 Hz.

4.3 Standard filter

In KAGRA a single standard filter is foreseen in the seven type–B attenuation chains, and 3 standard filters are used in the four type-A chains, for a total of 19 standard filters. The standard filter is a smaller version of the pre-isolator filter, enclosed by a cap that allows suspension of the filter from its center of mass. The filter is designed so that the working point of the filter falls close to the center of mass, so that the rocking modes of the filter body are at low frequency. Although the heads of the suspending and suspended wires are few mm apart, and the heads each 4 mm thick, due to the wire rigidity, the separation of the effective bending points is about 40 mm. As a result the standard filter rocking mode frequency is at 1-2 Hz. The rocking mode frequency can be lowered by changing the shape of the two wire receptacles to move the effective bending point below the filter's center of mass by an appropriate amount. The standard filter is provided with magic wands and with a LVDT/voice coil pair for diagnostic purposes.

No DC motorized correction spring is foreseen for remote adjustment of the working point. In Type–A only, DC adjustment is replaced by a thermal actuation scheme is provided. The thermal variation of the Young's modulus of the blade material (around -200 ppm/K for maraging) is exploited to finely tune the filter's working point. This is done by controlling the vacuum tank temperature around the filter with thermal pads. They consist in a couple of loops of 6 mm stainless steel tube tightly wrapped around the pipe, covered by thermal insulation. Stabilized temperature water is flown into the tubes. A Peltier heat pump between the input and output flow allow extra fine temperature tuning. The safety structure above and below the standard filters was designed to act as thermal baffles that define an individual thermal bath around each filter. The temperature is changed very slowly until the monitor LVDT reads the desired working point of the filter.

4.4 Eddy current damping stage

One of the most serious concerns in tall single wire suspension is the excitation of the torsion (yaw) modes of the wires. Single wire suspensions allow a suspended filter to be isolated in all six DOF. However, a long wire suspension becomes quite soft in rotation around the vertical axis. The wire torsion modes have extremely low resonant frequencies (<10 mHz in Virgo) and very high Q factors, therefore the decay time can be crucially long (hours). These modes are easily excited by mistakes of control actuation at the inverted pendulum level, or radiation pressure of the laser, and once they are excited one has to wait until they decay to sufficiently small amplitude for a new interferometer lock acquisition. Damping of the torsion modes is absolutely necessary for efficient operation of gravitational wave detectors. Virgo suffered from this problem and an external active damping system operating near the bottom of the chain had to retroactively implemented. In TAMA-SAS, an active control using photo sensors and coil-magnet actuators was implemented for torsion mode damping [30]. This method worked effectively and reduces the decay time of the torsion modes by a factor of 10 or more, while it is limited by range of photo sensors and therefore stops operating whenever large angular excursions occur. In order to avoid the above-mentioned problem in KAGRA-SAS, the torsion modes are damped passively by an eddy current damper mounted at the head of the chain. The damper also assists the action of the inertial damping in reducing the excitation of the other translational modes of the attenuation chain.

4.4.1 Eddy current damper design

An additional standard filter is inserted below the pre-attenuator stage for the specific purpose of providing means to damp the torsional resonances. A high conductivity, 10 mm thick, OHFC copper ring is bolted on the top surface of the filter (see Fig. 26). The magnetic part of the eddy current damper is composed by a heavy, soft iron ring suspended from the bottom of the pre–isolator by means of three wires. Its lower surface is loaded with clusters of 12.5 mm cube magnets.

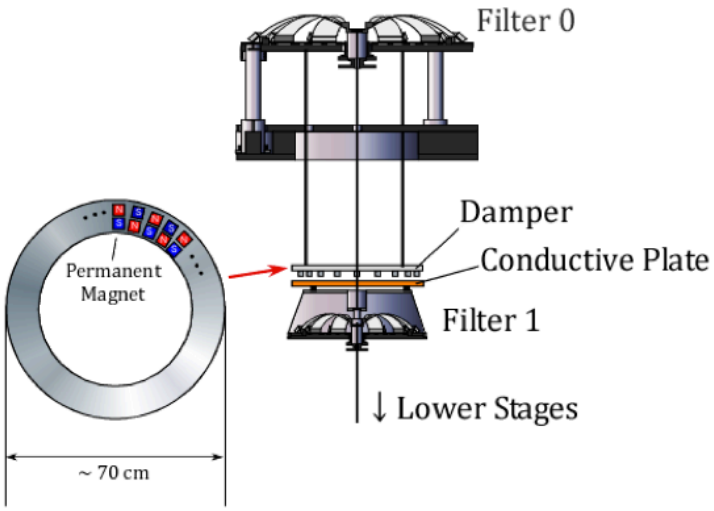

Figure 26: *Conceptual design of torsion mode damper.*

The magnets are in group of 4 or 16, with vertically oriented dipoles, 25 mm pitch and alternate polarity to cancel the dipole, quadruple and higher order fields at large distance while extending magnetic field loops with strong gradients 10 mm from their lower surface, but rapidly decreasing strength at larger distances. The copper ring is close enough to intercept a large fraction of the magnetic field loops. Any differential motion between the two plates produces braking torques. Although the damping torque is exerted only between the pre-isolator and the first stage, with a proper choice of wire torsional stiffness, the rotational motions of the lower stages are also damped. The positioning of the damper at the head of the chain eliminates any danger of feeding damper noise to the mirrors. The separation between the hovering magnets and the copper ring is tunable to change the damping strength. The type-A and type-B eddy current dampers differ only for the length of the disk suspension wires, from 955 mm in the type-B to about 1947 mm in the type-A. The cross-section of all suspension wires has been engineered in order to increase the torsional stiffness while preserving low

bending stiffness (see Fig. 27). In this way all torsional modes are coupled (i.e. recoil is observable) to the first standard filter, making the eddy current damper effective.

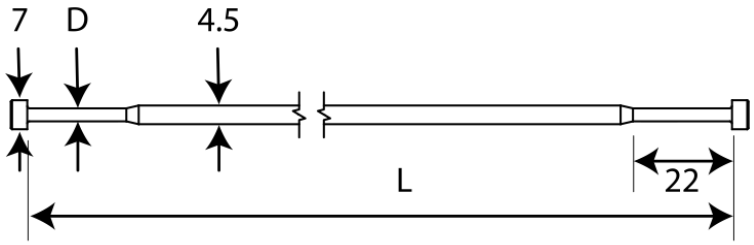

Figure 27: *Main suspension wire design; the wires are machined out of 7 mm diameter centerless ground maraging steel rods. They are provided with two 7 mm diameter nail heads. Below the head, a neck of variable diameter D extends for 22 mm length to the wire body,4.5 mm in diameter. In Type–A, the diameter D changes according to the wire's load, from 3.1 mm diameter (*7.1 mm^2 *surface) below the top filter to 2.2 mm diameter above the bottom filter. The different diameters are chosen to maintain the optimal stress a stress of* < 0.8 *GPa. The length L is chosen to match the separation between consecutive filters.*

4.4.2 Eddy current damper simulations

In order to evaluate the performance of the damper, a simulation with one-dimensional pendulum model was performed. After optimization of the wire's cross–sections, a substantial reduction of the decay times has been estimated for all torsional modes in the chain. Typical decay time scale is of the order of 1 minute, which is quite short considering that the period of the resonant modes are between 10 and 100 sec. Fig. 28 shows, for example, the simulated impulse torque response of the payload in Type–B chains with and without eddy current damper.

Actually, the eddy current damper affects not only on the torsion modes but also on the other pendulum modes of the chain. Fig. 29 shows a simulated transfer function of the horizontal displacement from the ground to the mirror in type-B system. The Q-factors of some pendulum modes are suppressed by factors of 10. These modes can be further damped by active control system on the top stage. Please note that the quality factors calculated for the damped modes represent are reliable upper limits because they derive from an easily achievable damping factor of the first stage. The quality factors without the damper are somewhat arbitrary. The quality factors of these pendulum modes are likely higher than shown in the graph, especially under vacuum conditions.

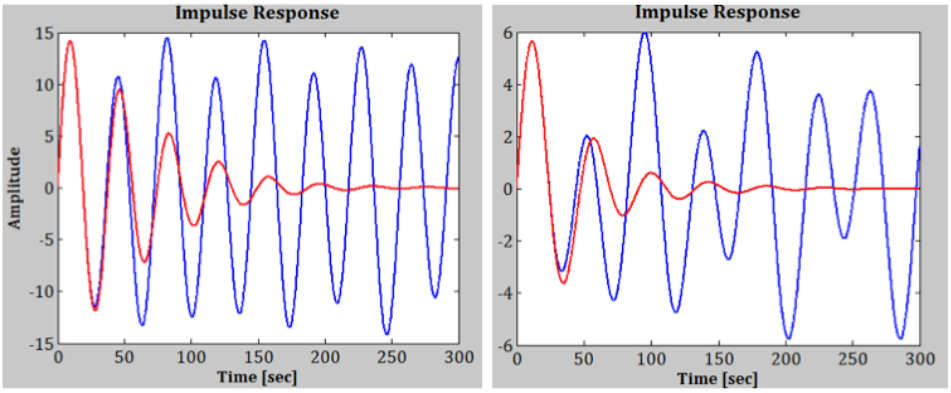

Figure 28: *Impulse torque response of the suspended payload in Type-B SAS. Left: recycler mirror, right: Beam splitter.*

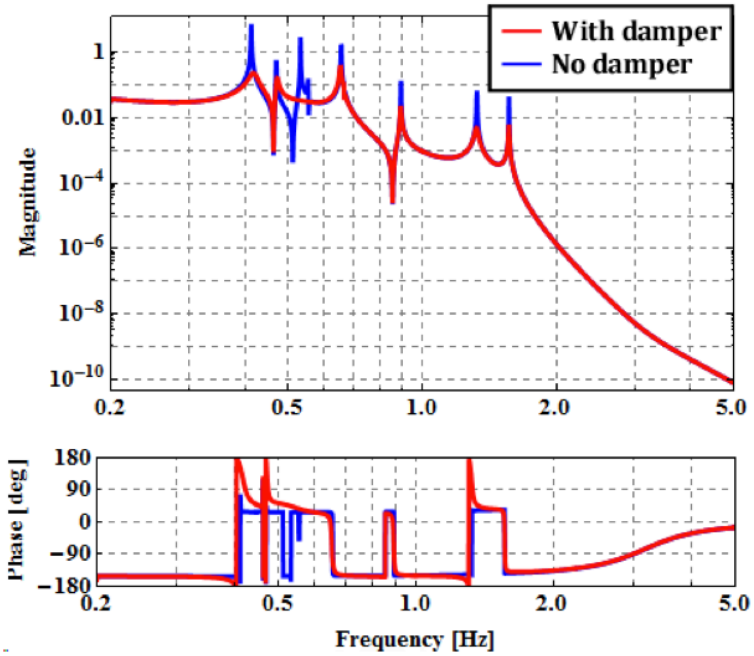

Figure 29: *Transfer function from ground displacement to the mirror displacement in Type-B system.*

4.5 Mirror suspension

The mirror suspensions (Fig. 30) and controls are formed by the bottom filter, suspending the intermediate mass (IM) and its recoil mass (IMRM), and the mirror with its recoil mass (MRM), both suspended from the intermediate mass. The mirror is controlled via electro-magnetic actuators from its recoil mass in the longitudinal, pitch and yaw degrees of freedom.

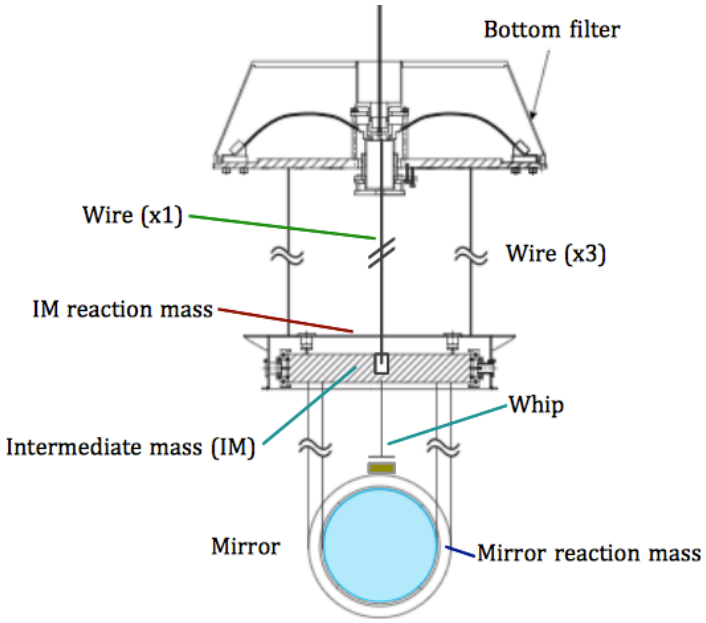

Figure 30: *Mirror suspension scheme. The intermediate mass (IM) is suspended with a single wire from the bottom filter. The IM reaction mass is suspended via three wires at 120 ° from the bottom filter plate. A concentric mirror/reaction mass arrangement, same as in Virgo and TAMA-SAS, was chosen to reduce couplings to the upper stages of the system. The IM is controlled by means of six OSEMs from the IMRM. Four OSEMs on the reaction mass are used to apply forces directly to the mirror. An eddy current damper, suspended with a wire from the IM, is used to damp the differential mode between mirror and reaction mass.*

The mirror actuation is limited to very low authority, to maintain actuation noise within acceptable limits. Slower and larger range actuation, in all 6 degrees of freedom, is possible actuating on the intermediate mass from its intermediate recoil mass, with electromagnetic actuators of larger force. Even lower frequency and larger amplitude movements are possible from the Inverted pendulum.

4.5.1 Bottom filter

The bottom filter (Fig. 31) of an attenuation chain is similar to a standard filter provides additional functions and therefore is substantially more complex. It provides:

- Suspension and seismic isolation of the intermediate mass
- Suspension of the intermediate recoil mass
- Static and dynamic vertical positioning of the intermediate mass with respect to its recoil mass
- Static tilt positioning of the intermediate recoil mass with respect to the intermediate mass
- Static yaw positioning of the recoil mass with respect to its recoil mass.

These functions are provided as follows:

- The intermediate mass is suspended from the keystone like a normal filter
- The intermediate recoil mass is suspended from the bottom filters by means of three wires at 120°. The intermediate recoil mass therefore tracks the tilt movements of the bottom filter.
- The static and dynamic vertical positioning of the intermediate mass with respect to its recoil mass is obtained via the voice coil actuator, and/or thermal tuning.
- The static tilt positioning of the intermediate recoil mass with respect to the intermediate mass is obtained by tilting the bottom filter by means of two manual and two stepper motor controlled tuning masses.
- The static yaw positioning of the recoil mass with respect to its recoil mass is obtained with a stepper motor controlled rotational mechanism similar to the one mounted in the keystone of the pre-isolation filter.

4.5.2 Intermediate mass and intermediate recoil mass

The mirror and its recoil mass are suspended from the intermediate mass, which is controlled by its reaction mass, with the former suspended by the bottom filter and the latter from the body of the filter (see Fig. 30) . The recoil mass has the shape of a box, encasing the intermediate mass. Sensing and actuation are collocated, made by means of six OSEMs, three on the top and three on the sides of the box. They are positioned to form as diagonalized action as possible:

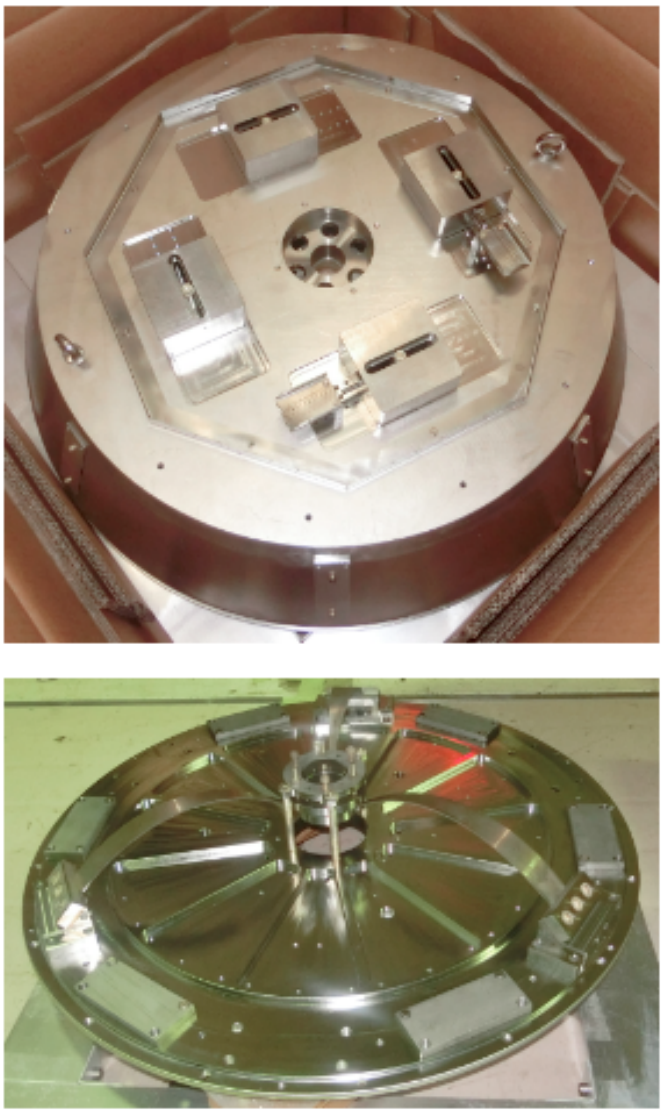

Figure 31: *Picture of the bottom filter prototype. Top: top view of the filter with the cap bolted in place. The static and motorized counterweights for the DC balancing of the mirror suspension stage are visible. Bottom: view of the filter with the cap removed.*

- The three horizontal actuators are as much as possible on the plane of the center of mass, to minimize tilt action. A single, centered actuator generates force along the beam line only. Two units are placed on opposite sides, one forward and one backwards, so that when operated with opposite polarity they generate a pure transversal force, and when operated with same polarity they generate a pure *yaw* torque.
- The three actuators on the cover are placed on an equilateral triangle, centered around the suspension wire, with one point aligned towards the beam line. When operated with same polarity they actuate in the vertical direction. When the two side units are operated with opposite polarity they produce pure *roll* torque, when the forward unit is operated with opposite sign than the back ones, and $\sqrt{3}/2$ force ratio, a pure *pitch* torque is applied.

The same argument is applicable to the collocated position sensors. Starting from a control matrix with a hardwired diagonalization vastly simplifies the problem of decoupling the different degrees of freedom in the control. The intermediate mass carries a whip loaded with a magnet matrix, designed to damp the mirror recoil mass modes, especially the bounce mode, which would otherwise be short–circuited on the mirror. This damping solution is viable and very convenient for beam splitter and recyclers, but it is not suitable for the four main mirrors, where the thermal noise from the eddy current dissipation would spoil the interferometer sensitivity.

4.5.3 OSEM

Position sensing and actuating between the intermediate recoil mass and the intermediate mass, and between the mirror recoil mass and the mirror are collocated and realized in a single device called OSEM (see Fig. 32), acronym of Optical position Sensor and Electromagnetic actuator. Position sensing is made with a shadowmeter, i.e. a LED shines on a photodiode light detector, and a moving flag generates an occultation proportional to the displacement. Actuation is applied by a 600 turn coil with 28–mm effective diameter acting on a permanent magnet 7–mm off center. The coil is mounted on the same fixed support of the Optek OP–232 LED and photodetector Hamamatsu S1223-01 (3.6X3.6 mm^2) while the magnet is mounted on the back of the occultation flag. The working point of the position sensor is when half of the LED light is occulted.

Typical achievable sensitivities are $10^{-9}\mathrm{m}/\sqrt{\mathrm{Hz}}$ at 0.1 Hz and $10^{-10}\mathrm{m}/\sqrt{\mathrm{Hz}}$ at 10 Hz. The length of the flag is chosen so that when the shadowmeter is at its working point, the center of the permanent magnet is 1/2 of a coil radius away from the center of the coil, to obtain the maximum of

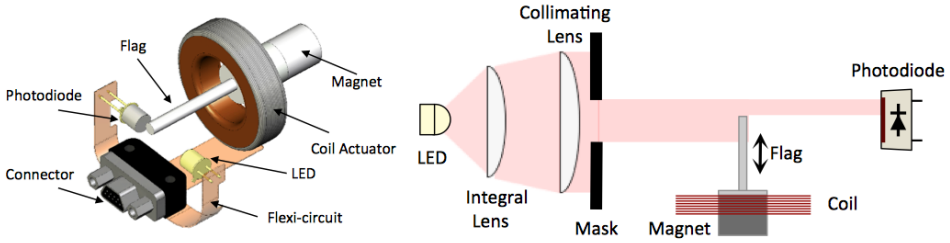

Figure 32: *Figure 5: Scheme of collocated shadow sensing and coil-magnet actuation in OSEMs [22].*

the force and the best force uniformity. For the intermediate mass a 10–mm diameter, 10–mm thickness NdFeB magnet is used to provide relatively large actuation force. At the mirror level, a 6–mm diameter, 2–mm thickness magnet is used to limit the actuation noise. The flag, the magnet stand and the coil body have been made out of PEEK. To avoid electrostatic charging problems Carbon fiber loaded PEEK was used as well. The resistivity of carbon loaded PEEK was measured turned out to be quite temperature dependent and not uniform, changing by $\pm 25\%$ on the scale of a centimeter around a value of 49 kΩ–mm. Nevertheless its value is high enough to fully avoiding interfering with actuation magnetic field via eddy currents. Because any metal loops near the actuation coils is susceptible to generate Eddy currents that would introduce frequency dependent delays to the control forces, great care was made to introduce appropriate cuts in the metallic structure of the recoil mass. In addition, to further reduce the Eddy current problem, the recoil masses were designed in titanium grade V, for its small electrical conductivity. For the same reason, the permanent magnets on the intermediate mass were mounted on rigid PEEK stands. Using PEEK for the magnet structure and flag has the additional advantage that the low quality factor of PEEK eliminates the possibility that the stand's own resonances introduce mechanical noise in the sensor signal. Of course this solution would not be suitable for any mirror susceptible to inject thermal noise contributions to the interferometer noise budget.

4.6 Mirror suspension prototype test

A full scale payload prototype was assembled at NAOJ (see Fig. 33) to verify assembling procedures and to test the active damping of the rigid body modes of the final stage of the Type–B suspension by means of OSEMs. The OSEMs mounted on the mirror reaction mass have first been characterized and calibrated.

The OSEMs were calibrated on an in situ made set-up consisting of a fixed

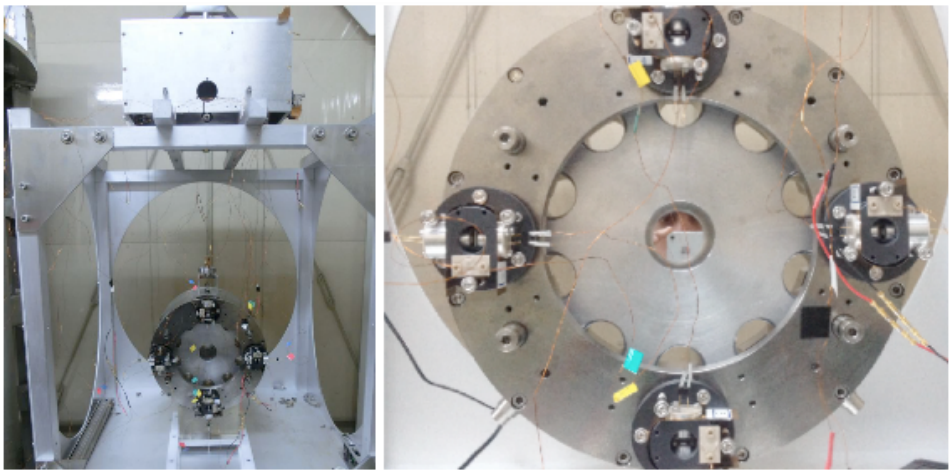

Figure 33: *View of the full scale mirror suspension prototype at NAOJ. On the right picture the four OSEMs, mounted on the mirror reaction mass, were used to control the modes of the suspension of a dummy mirror.*

rod to clamp the OSEM on and one 3 degrees of freedom translational stage. This set-up made it possible to secure the best possible level of orthogonality between OSEM and flag. Before each calibration run, the coupling to from movement in the other two degrees of freedom than the axis in which the flag is translated was checked and, if possible, improved by repositioning the OSEM in another angle. The couplings can be due to this non–orthogonality, but also by reflections inside the OSEM and how they relate to each other was unknown.

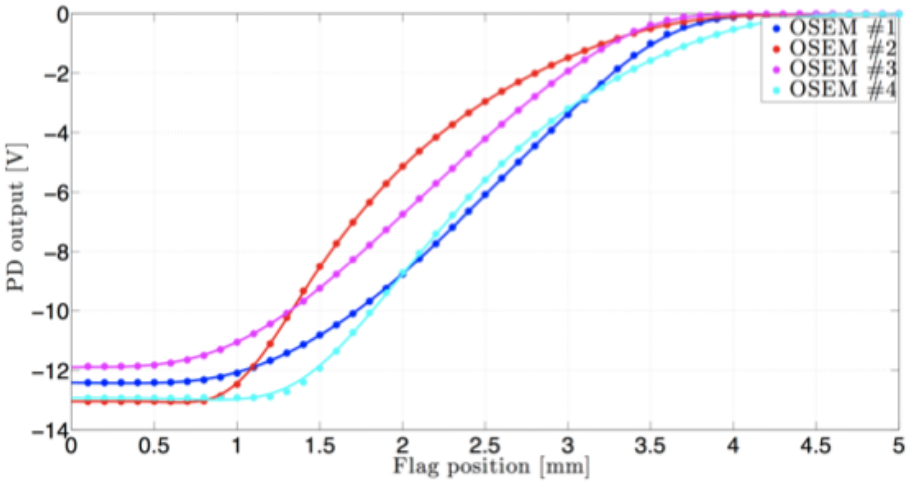

Figure 34: *Voltage vs flag position curves for the four OSEMs at the last suspension stage.*

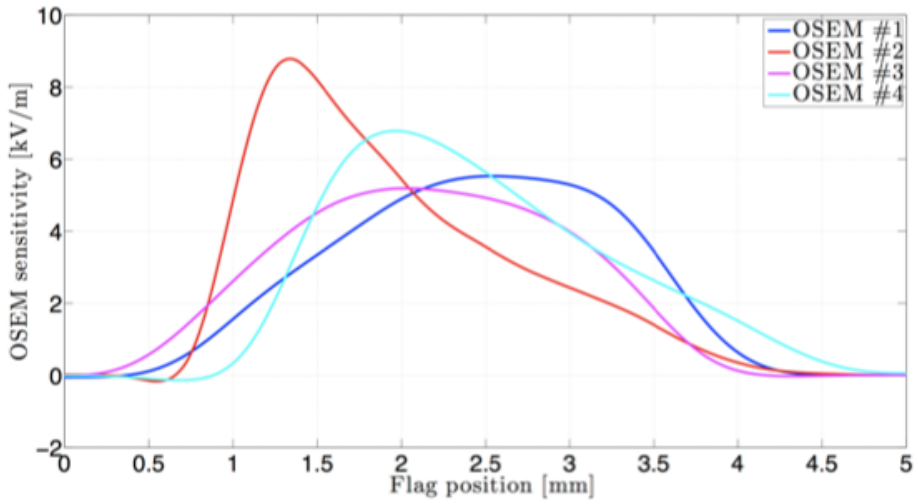

Figure 35: *Sensitivity vs flag position.*

Cutting trough the middle of the beam (see Fig. 34 and Fig. 35) ideally shows a constant gradient, as is visible for OSEM 1 between 2.2 mm and 3.3 mm. Across this linear range, the OSEM 1 sensitivity is about 5 kV/m. OSEM 2 most likely has its LED glued under an angle, so that the beam's intensity is less well distributed compared to OSEM 1 and OSEM 3. Noise measurements of all OSEMs were performed and, using the sensitivity figures, typical values were determined at 1 Hz of about $7 - -9 \cdot 10^{-9}\mathrm{m}/\sqrt{\mathrm{Hz}}$ and $1 - -2 \cdot 10^{-10}\mathrm{m}/\sqrt{\mathrm{Hz}}$ at 10 Hz. , The test mass and the reaction mass were then suspended and the OSEMs were attached such that their outputs were reading off voltages corresponding to the middle of the flag position interval where the sensitivity (gain) was maximum. Control of the mirror position along *longitudinal* and the two *tilt* axes has been implemented by using the CDS real time digital control system [ref]. Sensing and driving matrix were diagonalized first; after a few iterations, couplings between the three degrees of freedom were reduced below 1% level. A simple derivative feedback was engaged.

Fig. 36 shows the open–loop and closed–loop response along the suspension longitudinal axis after a simple derivative feedback was engaged. The unity gain frequencies, indicated by the red lines in the open–loop plot, show that the feedback loop is controlling only at frequencies around the 0.65 Hz resonance frequency efficiently damping the fundamental pendulum mode of the suspension.

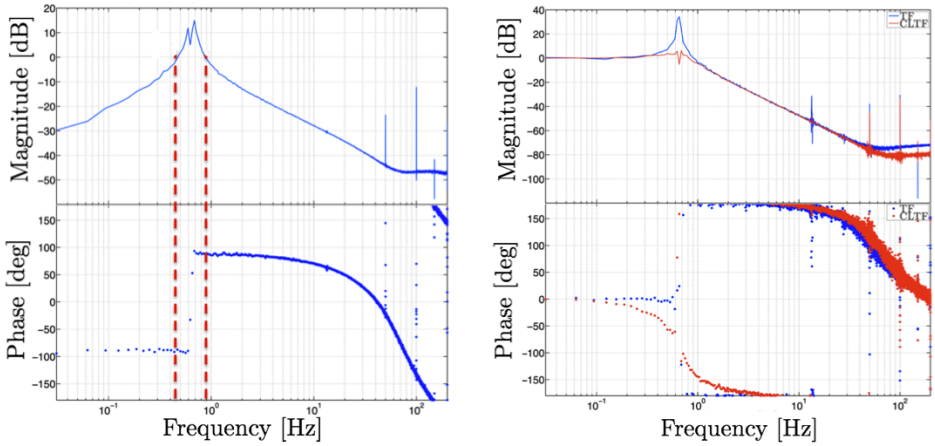

Figure 36: *Open–loop (left panel) and closed–loop (right panel) response measured along the longitudinal degree of freedom. The pendulum mode is efficiently damped. A negligible spurious coupling to the 14 Hz vertical bouncing mode of the suspension can be observed. The plateaus, visible from 50 Hz onwards, have been attributed to electromagnetic coupling between the currents running to the coils and coming back from the photodetector.*

4.7 Optical levers: design and prototype test

Based on the successful scheme implemented in Virgo, sensing for the angular alignment and damping during interferometer lock acquisition and will suitably be provided by a set of optical levers (local control). Long life time and stable light is desired for the light source of optical lever. To meet such requirement, a fiber coupled superluminescent diode (SLD) has been selected as the light source. Power of 1 mW is sufficient in the case of about 30% reflectivity of the mirror. The life time of SLDs is expected to be more than 10000 h. Temperature control can be mounted on the SLD unit in the fiber coupled system. This brings a high stability of laser power by avoiding mode hopping. Moreover an optical fiber with a rigid collimator lens system can make the light source stable against vibration, easy to setup even in a small area, and easy to replace in case of failure. In using optical fiber coupling, interference between the core beam and reflection light from cladding may cause severe fluctuations of the beam spot. The SLD, that has short coherence length (about 50 nm) also suppresses these effects. Polarization maintaining (PM) fiber is used to mitigate fluctuations of the received total power caused by polarization rotation of the launched beam (the beam has a large incidence angle on the target mirror, especially in Type–B suspensions with about 45 °. FC/APC connector is used to mitigate optical feedback from reflected light that could cause power instabilities. During

installation phase a red (around 670 nm) wavelength SLD will be adopted to speed up the initial alignment. After the commissioning of the suspension systems, it could possibly be replaced with an infrared SLD, known to have longer life time. Position sensitive detector (PSD) is selected as a photo receiver because of its broader linearity compared to quadrant photo detectors (QPDs) and to its output insensitivity to the spot size (spot size only affects the width of the linear range). Nanometer noise level in the spot centroid position measurement can be achieved. The broader range is necessary for the yaw motion of the mirror in KAGRA suspension system that employs a single wire suspension. Even in the short length optical lever planned for Type B and C suspensions, it is difficult to make a small spot size with few meters working distance by commercial and reasonable collimator lenses. Thus the spot diameter is tuned to about 2 mm by means of an adjustable collimator lens. Note that different design of collimator lens and construction will be needed in the long length optical lever for Type A suspension. The condition of the launching and receiving pads is significant for a stable operation of optical lever. The pads (optical breadboards) and optical windows should be covered by windshields to protect the beam line from air flow and dusts in air. For some vacuum tanks, pylons will be prepared to put the launching and receiving pads. In vacuum tanks for Type B and C, the incident angle of the optical lever is large (45 degree), causing the optical lever output to be sensitive to the longitudinal motion of target mirror i(see Fig. 37 left panel). To separate angle and longitudinal motion, the *turning* method is used (see Fig. 37 right panel).

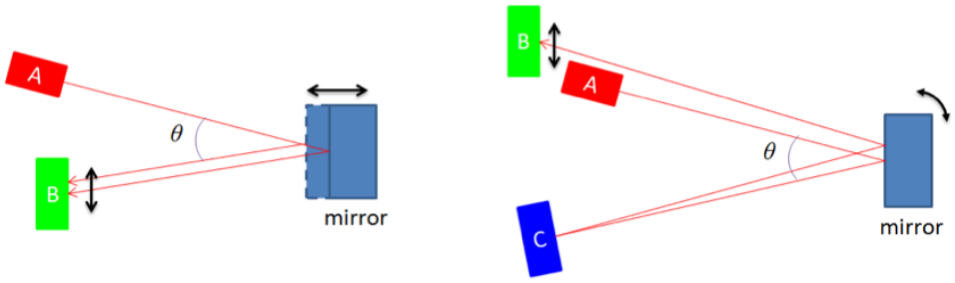

Figure 37: *Length coupling and turning method. A: light source, B: position sensor, C: turning mirror.*

If the turning mirror is replaced with a beam splitter (BS), the transmitted light can be also used for length sensing. As shown in Fig. 38, the turning port has some options for additional motion sensor. In the case of option 1, the signal includes not only angular motion but also longitudinal motion of mirror. The longitudinal motion signal can be separated from angular motion using the signal of the PSD in the input port. In the case of option 2, the longitudinal motion and broad range angular motion can be obtained

using focal plane and image plane, respectively [31] [5].

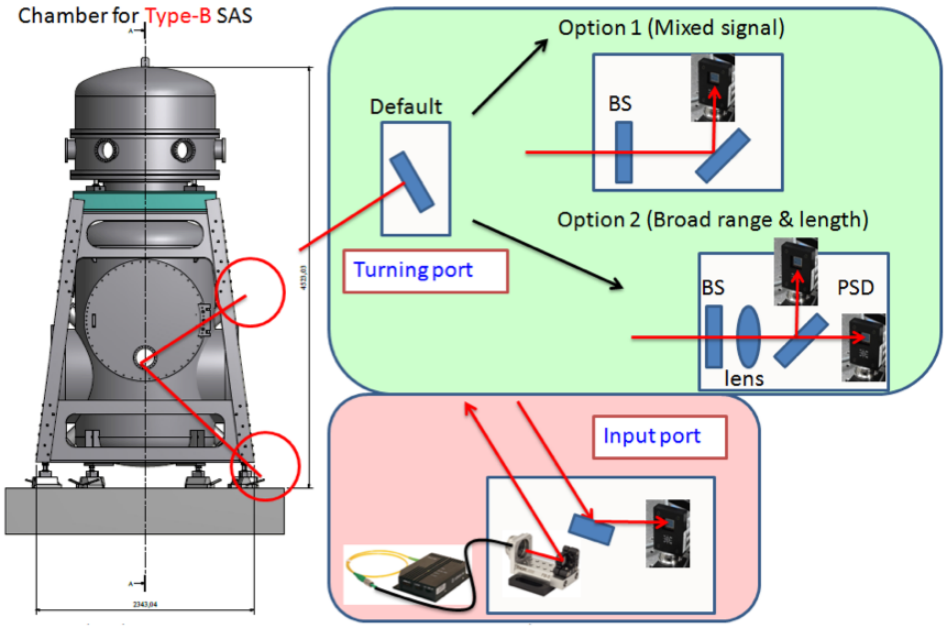

Figure 38: *Layout design and option scheme.*

A full scale prototype of an optical lever for Type–B suspensions was assembled and tested at NAOJ (see the layout in Fig. 39).

Long–term stability of the beam spot was evaluated in this preliminary test. The PSD output was sampled at 0.25 Hz sampling rate for a few days. Large temperature changes (about six degrees during this measurement), due to lack of power of the air conditioning in the experimental room, characterized the data.

From the fit of data in Fig. 40, the optical lever output has a temperature response of 8 μm/K superimposed to constant drift of 14 μm/day in X direction, while in Y direction the temperature response was 50 μm/K superimposed to a constant drift of 170 μm/day. The measured sensitivity to temperature changes is not considered a serious problem due to good temperature stability (within $\pm$0.2 K) expected in the Kamioka mine. The constant drift found in this preliminary measurement is three times worse than the requirement, (spot drift should never exceed 60 μm), can be solved problem because it is not difficult to find a fringe of the cavity by shaking the mirror in the case of factor of three worse drift.

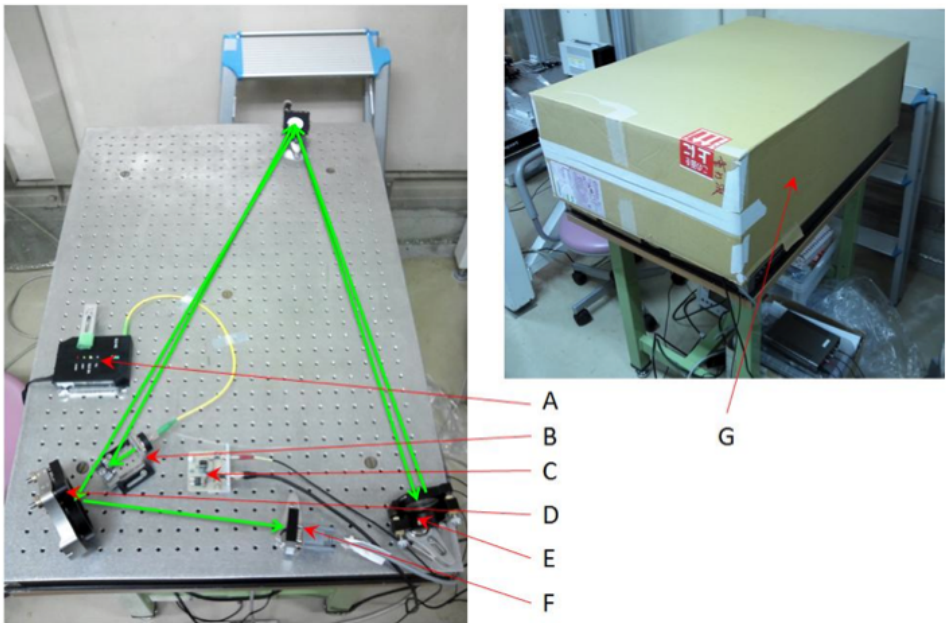

Figure 39: *Photograph of the prototype assembled on top of an optical table. A: SLD unit, B: launcher with collimator lens, C: thermometer, D: steering mirror, E: reflection port mirror, F: PSD, G: wind shield.*

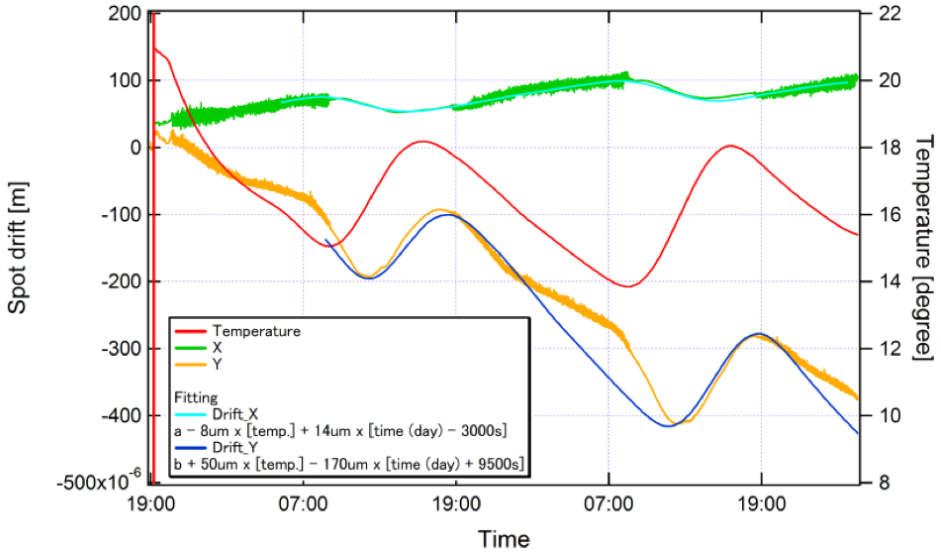

Figure 40: *Spot position drift measurement in the prototype.*

5 Software modeling of KAGRA suspension system

In order to fully exploit the advantage of installing the seismic suspension in underground environment KAGRA has developed its own modeling tool. The software implemented by T. Sekiguchi [11] at ICRR was initially developed to assist the mechanical design of the suspension. In fact, due to the need of suitable control systems, meant to operate the interferometer and to damp the mechanical elongation at the frequency of internal modes, it was clear from the beginning that the development of a multipurpose tool allowing technical noise projections and closed-loop operation was the ultimate target of this effort. During the preliminary phases the tool developed by KAGRA was checked with respect to other modeling tools developed within Virgo and LIGO collaborations, then, it became the main platform for the projections fully dedicated to KAGRA. All the results worked out are widely discussed within the collaboration and used to drive the final implementation. The overall performance of passive mechanical system and its frequency response to the external/internal force/torque are investigated by simulation with rigid–body modeling. The suspension system is resolved into rigid bodies and elastic components (such as cantilever springs and wires). The equations of motion are constructed from Lagrangian and are linearized around the equilibrium position. Imaginary parts of the spring coefficients are added to introduce structural damping and calculate suspension thermal noise. Heat links in cryogenic payload are also assumed as elastic springs in the model, while they have internal modes above few Hz, which enhances the vibration transmission at high frequencies. In order to take into account the effect of violin modes of the heat links, the spring coefficient of the heat link is assumed to be frequency-dependent. The frequency dependence of the spring coefficient is calculated by finite element analysis tools (COMSOL *Multiphysics*). Once the rigid-body suspension model it constructed, it is converted into a linear state-space model and inserted to a local control model of the suspension. The servo filters of the feed-back control are designed, and impacts from sensors and actuator noises are investigated to set the requirements for the electronics noises. The block chart diagram of modeling the suspension system is shown in Fig. 41.

The mechanical model makes use of *Mathematica* core that works out matrixes of transfer functions for any DOF of any stage to any other DOFs of any other stage. Mechanical noise can be injected from the ground at several stages, the main one are the pre-isolator horizontal and vertical and the payload, through the heat link, a mechanical shortcut, modeled through FEA, with the inner side of the cryostat hosting the payload. Once the matrixes of transfer functions are computed the mechanics is ported to state-space

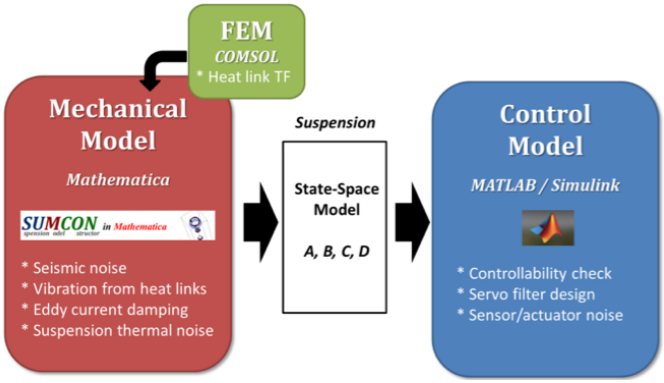

Figure 41: *Block chart of the modeling tool.*

model that is used by a *Matlab* section dedicated to closed-loop studies whose chart is sketched in Fig. 42.

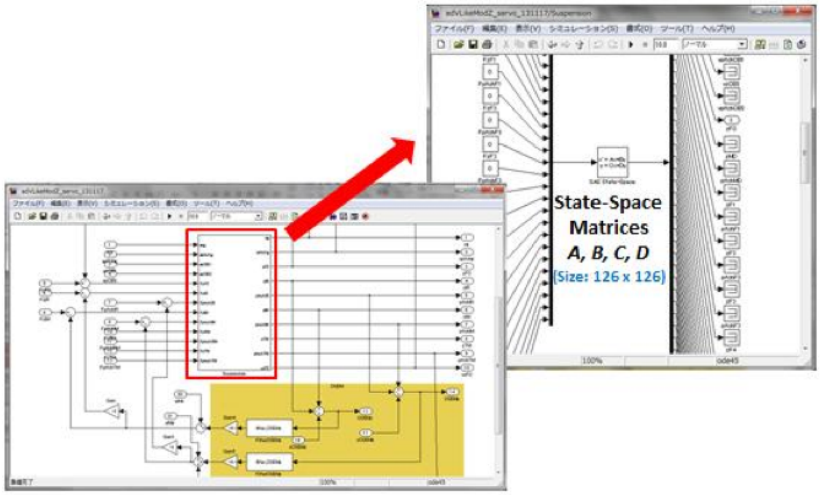

Figure 42: *Simulink model of the suspension with feedback controls.*

The choice of the affordable studies is large using this tool:

- transfer function matrices as functions of various mechanical parameters o coupling among payload DOFs
- passive, eddy current damping implementation
- control loops implementation
- suspension thermal noise projection
- noise projections of cryostat vibration

In the following we focus on mechanical issues related to ground disturbance and its attenuation.

5.1 A target study: suspended mirror position accuracy in Kamioka site

In order to acquire and keep the lock of the interferometer, RMS displacement or velocity of the test mass mirrors must be suppressed. The target RMS displacement of test masses in the absence of the global control is 100 nm. The RMS displacement of the ground motion in Kamioka Mine is typically smaller than 100 nm, but it can get larger depending on the oceanic activity. During stormy days (see blue line in Fig. 1) it may reach about 2 μm. In order to operate the interferometer stably in a long term, one needs passive or active attenuation of seismic noise around micro-seismic peak. Detailed simulations have been performed [32] assuming, conservatively, a ground vibration spectrum characterized by an extremely large micro-seismic peak, which is observed at Kamioka Mine during stormy days. Even if non–exhaustive, the results worked out through the modeling tool represent a milestone in the assisting the implementation of the overall suspension system. A rigid-body modeling tool in *Mathematica* is utilized to simulate the mechanics of Type-A SAS. A first set of parameters for the simulation was directly derived from the seismic suspension mechanical design and a preliminary version of the cryogenic payload system, reasonably close to that whose deign is about to be frozen by the KAGRA collaboration [33] during the delivering of the is document. The payload and its mechanical connection with the upper suspension stages and the radiation shield of the cryostat are sketched in Fig. 43 [34].

The parameters implemented in the model commented in the next sections are almost same as those in [33], but two different are used:

- IP is tuned at 50 mHz instead of 30 mHz.
- The suspension point of IM (Intermediate Mass in Fig. 43) is tuned so that the resonant frequency of IM pitch mode is 300 mHz. Low frequency tuning is required for alignment control of the mirror from IM stage.

5.1.1 Suspension mechanical response

Fig. [44, 45, 46] show frequency response of Type–A SAS to various excitations. The IP stage becomes more sensitive to the DC ground tilt when it is tuned at lower frequency. In the current design, the coupling factor is about 100 m/rad.

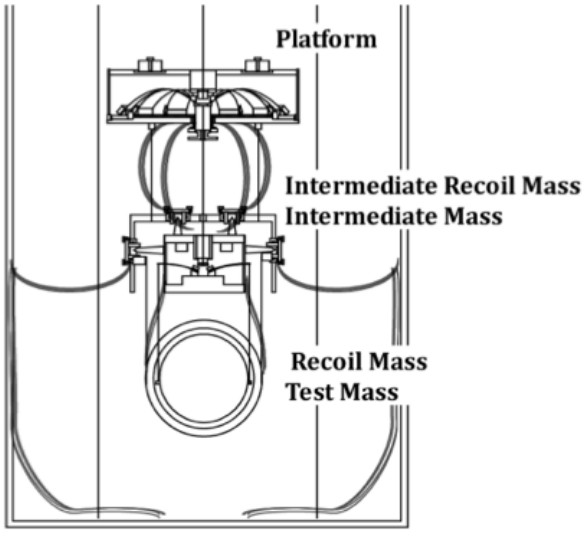

Figure 43: *Cryogenic payload design as assumed for the preliminary studies of the overall performance of Type-A suspension of KAGRA. The final design is conceived by KAGRA as close to this conceptual design. The radiation shield surrounding the payload is connected via 8 soft heat-links to the payload.*

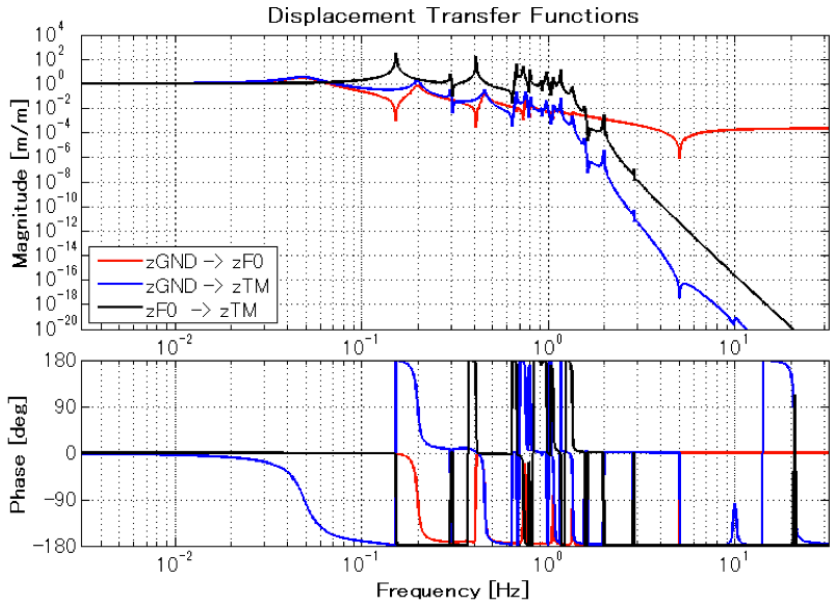

Figure 44: *Displacement transfer functions from ground translation to F0 and TM translation (red and blue lines). The black curve shows the ratio of two curves.*

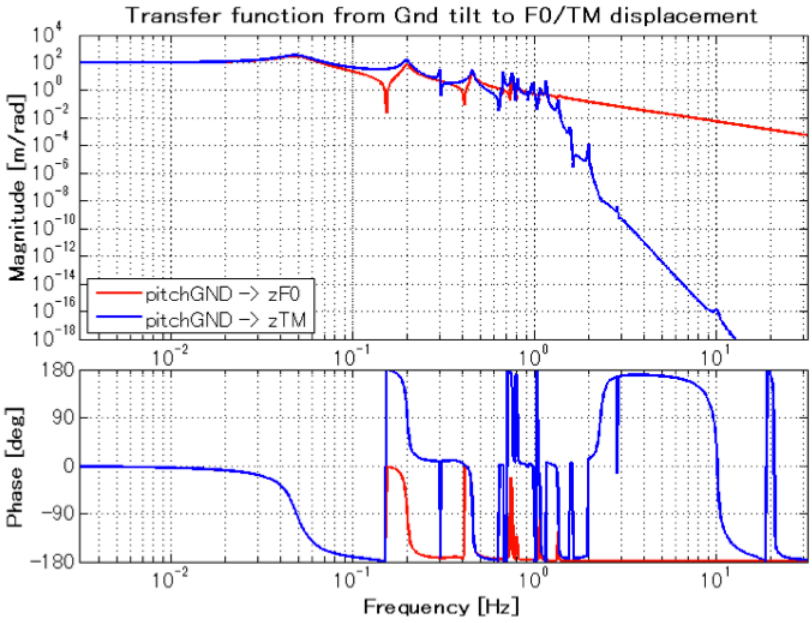

Figure 45: *Transfer functions from ground tilt to F0 and TM translation.*

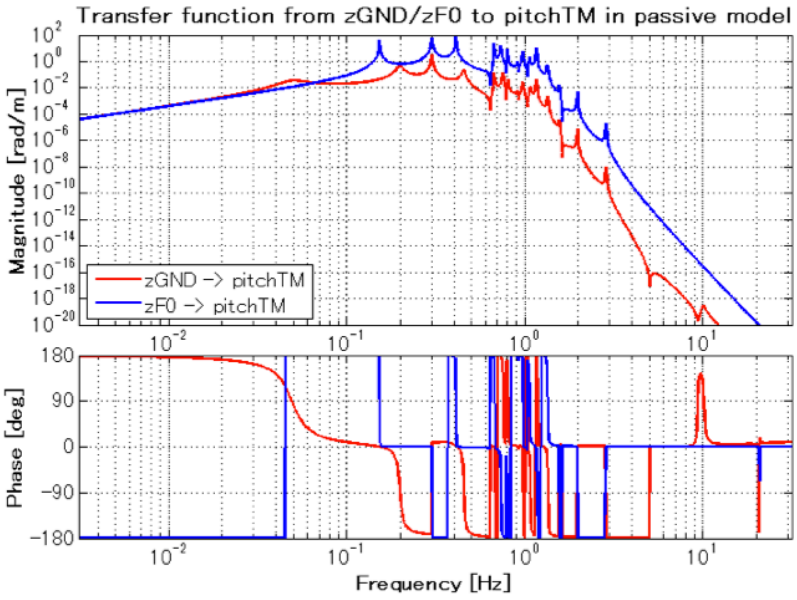

Figure 46: *Transfer function from the ground /F0 translation to the test mass pitch rotation.*

5.1.2 Sensor blending

Blending pre-filtering are derived from polynomial calculus in order to accomplish the damping of its internal modes and its position control through the devices located at the suspension top-stage (F0). The blending is a common practice in Virgo in order to reject microseism noise through the position sensor and to limit low frequency noise (tilt) due to inertial sensors [35]. For example, 5^{th} order blending filter is expressed as follows:

$$H_{HP} = \frac{s^5 + 5s_0s^4 + 10s_0^2s^3}{(s+s_0)^5}, H_{LP} = \frac{10s_0^3s^2 + 5s_0^4s + s_0^5}{(s+s_0)^5}, \tag{12}$$

where s_0 represents the blending angular frequency. Since the sum of two filters is unity, no phase lag would occur at cross-over frequency. KAGRA seismic suspension is assumed to be controlled by inertial velocity (Sercel L4–C geophones) and position (LVDT) sensors (see Fig. 47).

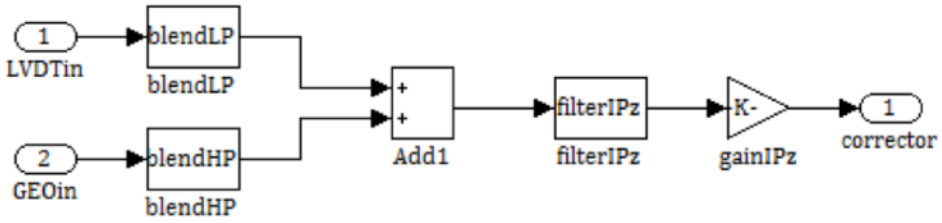

Figure 47: *Sensor pre-filtering and servo block.*

The blending filters used in the following simulation are based on the 5^{th} order polynomial with blending frequency at 40 mHz, but it also contains some featuring meant to reduce the microseism noise re–injection through the suspension transfer function, the comparison with respect to a simple polynomial blending is shown in Fig. 48.

5.1.3 Closed–loop projection and control accuracy

If one assumes a PID control similar to that applied in Virgo, readapted to KAGRA suspension design and employed velocity sensor instead of accelerometer, the preliminary result obtained is resumed in Fig. 49.

Provided that the spectrum that is considered is that of quite a noisy day, indeed that the seismic noise RMS at Kamioka site would be most of the time 10 times smaller, we see in Fig. 49 a significant attenuation of the microseism through position sensing can be easily achieved. The attempt

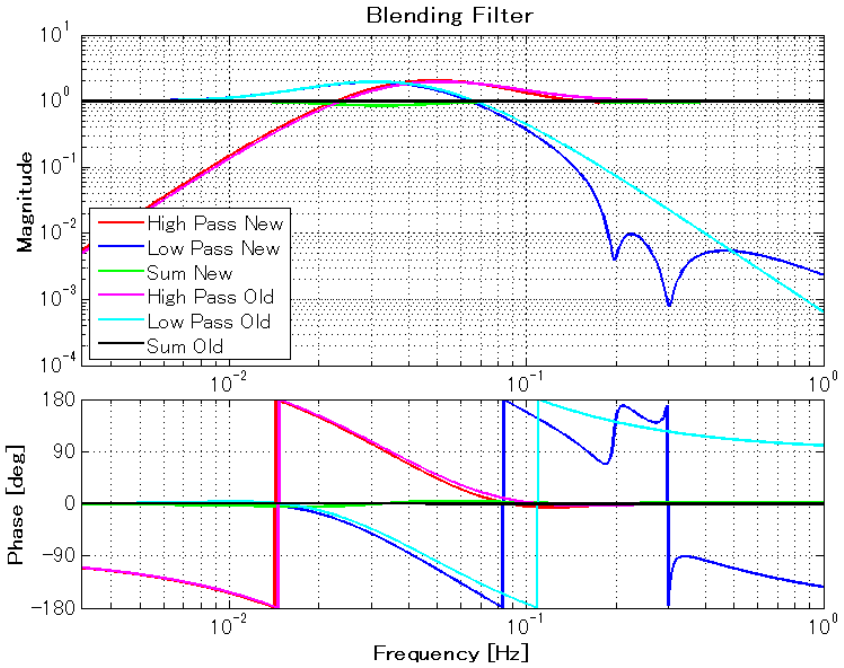

Figure 48: *Featuring the standard performance of polynomial blending meant to further reduce the impact of microseism though position control, provided the simulated transfer function of the seismic suspension.*

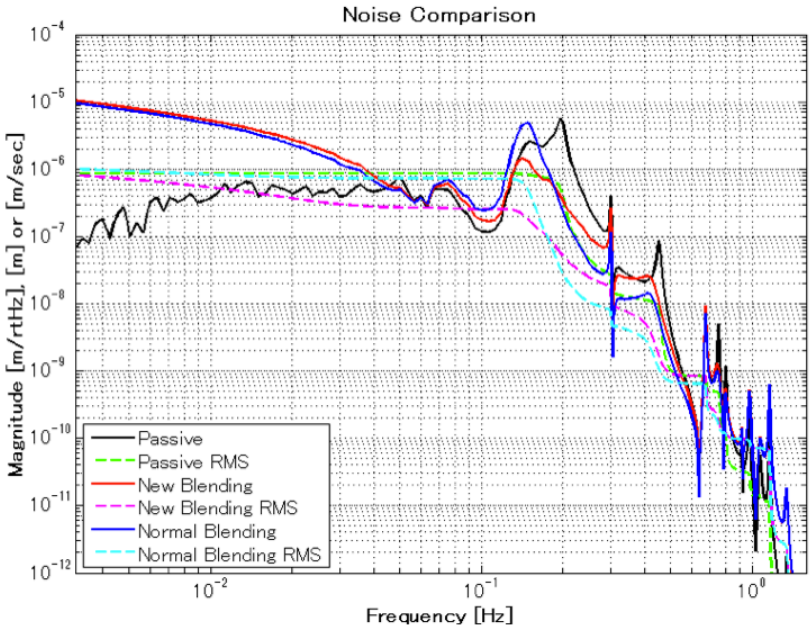

Figure 49: *Preliminary noise comparison through sensor blending.*

of fulfilling the requirement of 100 nm during stormy days implies a further improvement in the accuracy of suspension control. Further featuring of the blending is possible, but the most crucial component of the noise budget arising from the preliminary analysis performed by Sekiguchi *et al.* [32] is that arising from geophone sensing.

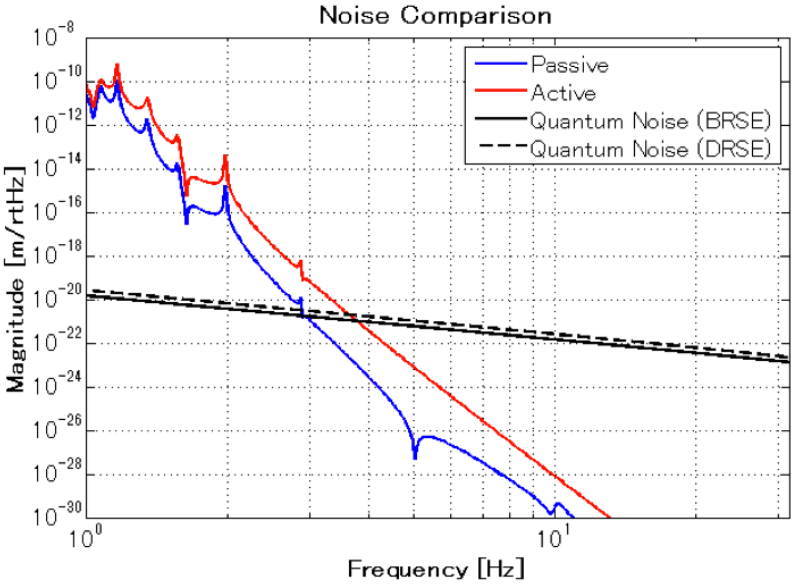

Figure 50: *Preliminary noise comparison through sensor blending.*

Test mass displacement noise, from the top stage horizontal vibration of passive and active system is shown in Fig. 50. An important indication arises as, although the control enhances the high frequency vibration, above 10 Hz, that is well below the target sensitivity.

6 Interfacing a SAS chain with a cryogenic payload

The original design of the cryogenic part of KAGRA's test mass suspension (see Fig. 51) does not include any vertical compliant element.

As a consequence:

- parasitic seismic vibrations transferred via heat links may damage the performance of the main attenuation chain.
- vertical thermal noise originating in the last SAS filter stage, at room temperature, reaches the mirror without any attenuation. Part of it will couple to its horizontal motion.

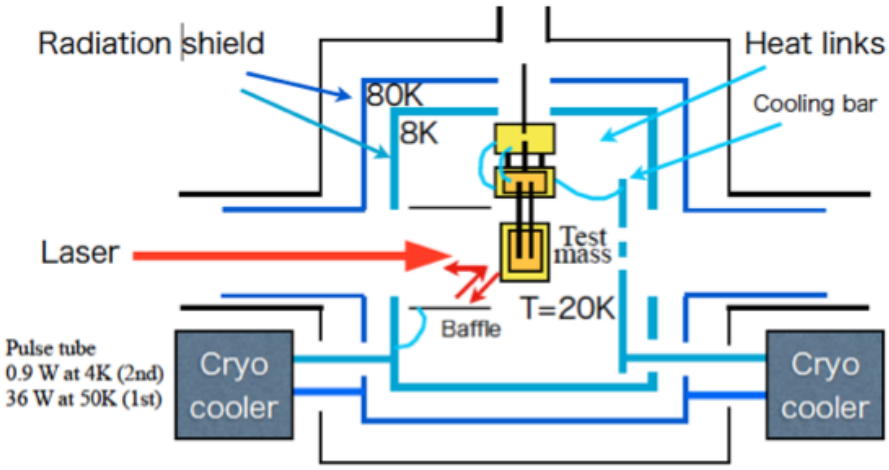

Figure 51: *Sketch of the mechanical connection of the payload with the radiation shield of the cryostat as in the original KAGRA design. The heat link from 8 K radiation shield is connected to the IM recoil mass and then anchored to the body of a vertical rigid cold platform.*

- the geometry of the mirror suspension fibers, 300–mm long 1.6–mm diameter sapphire rods, needed for heat transport reasons, is shifting the vertical mirror modes up into the detection band, while the violin modes shift down into the most sensitive region, when compared to a room temperature suspension.

The search for a better suspension of cryogenic interferometers like KAGRA and ET–LF leads to the need for cryogenic compliant elements. Solutions proposed so far (Fig. 52) include at least two stages:

1. a low-frequent upper stage, typically a sub–Hz GAS filter
2. a high–Q, high thermally conductive mirror suspension (about 10 Hz), typically blade springs or compressed beam springs made of sapphire, silicon or tungsten.

In this section heat link noise projections will be presented and design/feasibility issues towards a cryogenic sub–Hz GAS filters are discussed.

6.1 Heat link vibration noise projection

The impact of vertical component of seismic noise at Kamioka Mine site, passed through the mechanical transfer function of the KAGRA cryostat, as measured by KAGRA team at Toshiba Keihin Product Operations, Yokohama-city in 2013 and, then, through the transfer function of the thermal link path

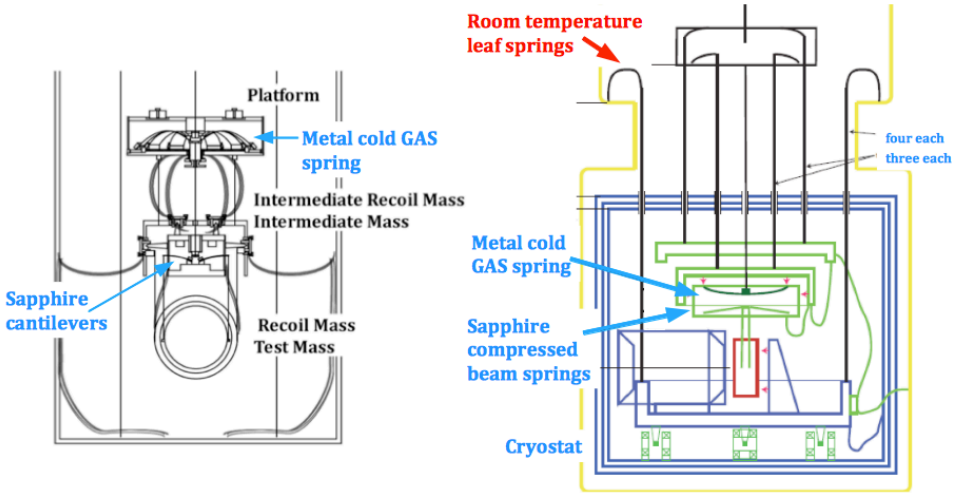

Figure 52: *Conceptual scheme of solutions proposed to mitigate issue caused by the vertical stiffness at the level of the cold stage. Left: a cryogenic GAS filter supports IM, IM recoil mass, TM and TM recoil mass to filter out vibrations from the heat links and to reduce vertical thermal noise level [34]. Right: room temperature springs support a massive cold platform serving as vibration isolation stage for heat link and cold baffles and as actuation platform for mirror local control during interferometer lock acquisition and as seismic isolation [36]. A reversed cryogenic GAS spring mounted inside the IM provides vertical compliance to it; sapphire compressed beam springs provide vertical compliance to the test mass.*

was estimated by means of dedicated transfer function measurements [37] [38]. Although the level of the upper cryogenic stage is assumed to have resonant frequency at 0.5 Hz and is significantly massive, the projection shows a significant impact of the vertical seismic noise above the nominal sensitivity. The plot in Fig. 53 shows the result of the simulation for the configuration shown in Fig. 52 left panel.

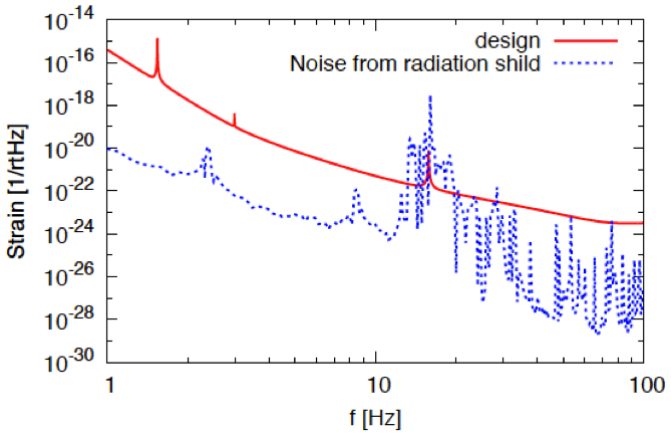

Figure 53: *projection of KAGRA site vertical component of seismic noise through the cryostat transfer function and reaching the payload and affecting the test mass position.*

Hence, while demonstrated the feasibility of a vertical filter equipped with cryogenics compatible anti-spring system, such to be tuned at 0.5 Hz and compatible with cryogenic drift, a further passive ancillary mechanical filter located to the radiation shield of the cryostat might be a viable solution meant to further mitigate the impact of the seismic disturbance before the connection to the payload[39]. By using the modeling tool described above, it must be remarked that interesting projections concerning the thermal noise can be derived. Indeed, given the geometrical vertical–to–horizontal coupling that affecting the setup of KAGRA test masses, the mechanical dissipation of the cryogenic vertical filter must be rather small, leading to an estimate of its quality factor at least 10 times larger than that of a typical of room temperature standard stage.

6.2 Feasibility of a cryogenic GAS filter

6.2.1 Vertical spring design scaling laws

The designer of spring blades for usage at high static stress can benefit from some simple dimensioning rules prior to elaborate FEM modeling. The

problem of suspending a mass M from a number n of cantilever blades of a certain shape and material with given Young modulus E and maximum allowable stress σ_m, at some desired resonance frequency ω_0, can be solved with the help of the expressions (scaling laws) summarized in Fig. 54. Design parameters as minimum blade thickness t and length L can be easily calculated. It is clear that suspending a larger mass requires a larger thickness or a stronger material, and possibly more blades. The length is scaling inversely proportional to the resonance frequency. The crucial material parameter involved is E^2/σ_m^3. The dimensionless factors S only depend on the blade shape and the four aspect ratios that characterize the geometry of the loaded blade. The examples given in Fig. 54 show the shape factors for uniform and triangular blades. Shape factors of more complex profiles and at large deflections can be obtained from numerical or FEM calculations.

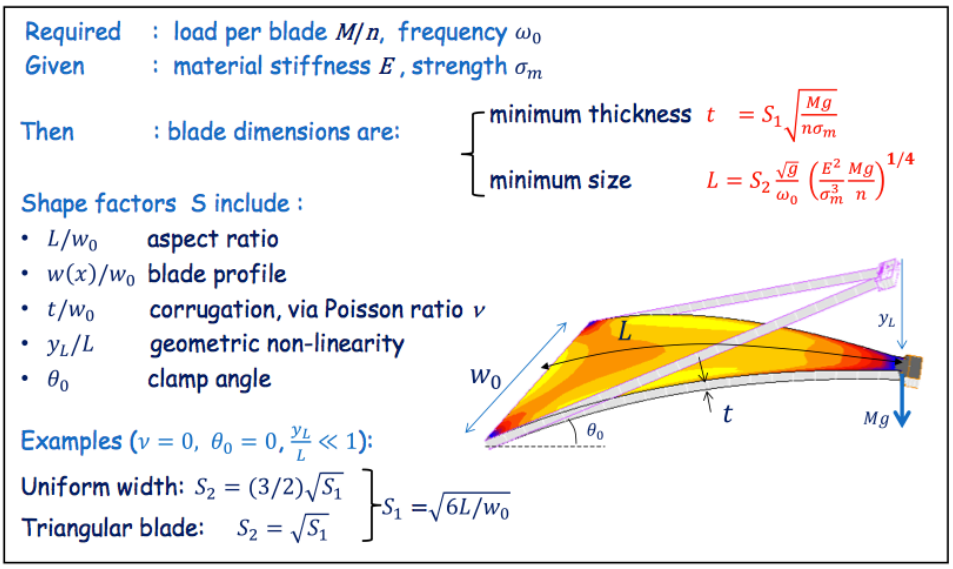

Figure 54: *Clamped cantilever spring dimensioning rules.*

The geometric anti-spring (GAS) blade (Fig. 55) in its so-called working point has a radius of curvature of the same order of magnitude as its own length. So it is by nature a geometric non-linearly deformed system. The only difference with the cantilever analysis is the horizontal, compressive force, putting the spring close to a critical compliant state of buckling. The compressive force is typically about three times the vertical load. Around this state you can realize a spring curve, the blue one, that shows an almost zero differential stiffness in the working point. The dimensional analysis in this case does not deliver the minimum required thickness for a given load, but the maximum allowed thickness for a given size. Also, the required spring size L is not governed by the frequency. Moreover, the length is

more sensitive to the material strength than the cantilever: it scales with a different exponent for both the material factor and the load per blade.

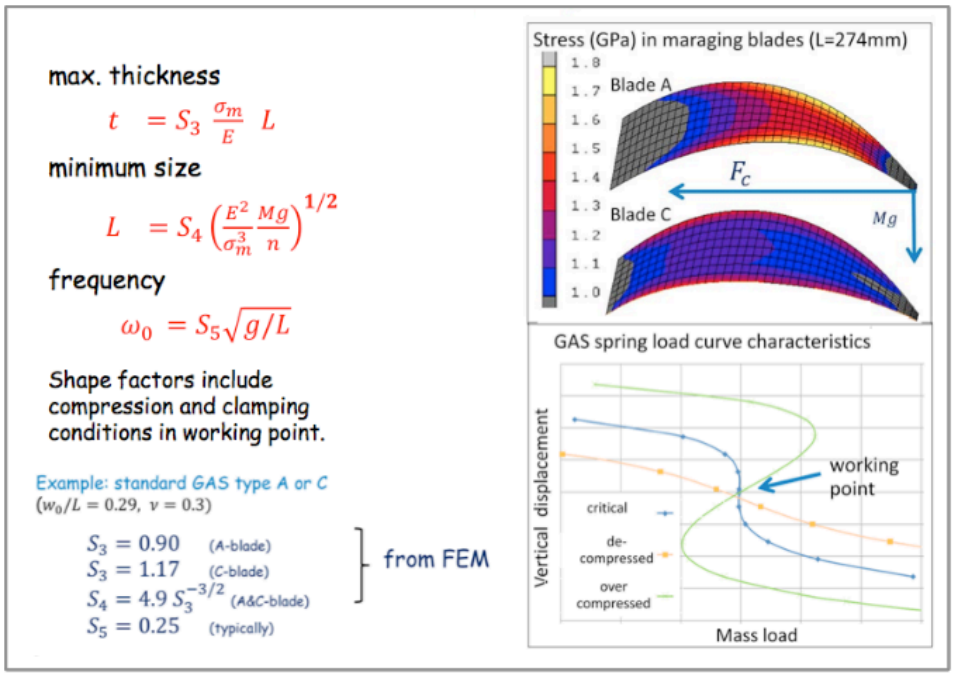

Figure 55: *GAS spring dimensioning rules.*

Fig. 56 shows the same formulas again, but now they express the mass that a blade of certain shape S can carry. Clearly for both blade types the load capacity has the same dependency on the material stiffness and strength. This allows to directly compare materials. Putting in some numbers gives the diagram that shows the blade spring load capacity of several metals, compared to some reference material, which is the maraging steel used for the SAS GAS filters. For instance, a Nispan-C blade (Nickel-Iron-Chromium Alloy) can only carry about 1/3 of a maraging blade of the same shape, and size, while glassy metal has a 1.6 times larger load capacity. Unfortunately glassy metal blades are not yet available in large enough size.

6.2.2 Effects of small thermal fluctuations on GAS springs.

The relevant material parameters are the thermo-elastic coefficient $\gamma = 1/E \cdot \partial E/\partial T$ and the thermal expansion coefficient $\alpha = 1/L \cdot \partial L/\partial T$. Their effect on the filter behavior close to its working point are described by the three expressions in Fig. 57. Analysis and measurements on Advanced Virgo EIB–SAS are in almost complete agreement. They show (see Fig. 57 bottom right

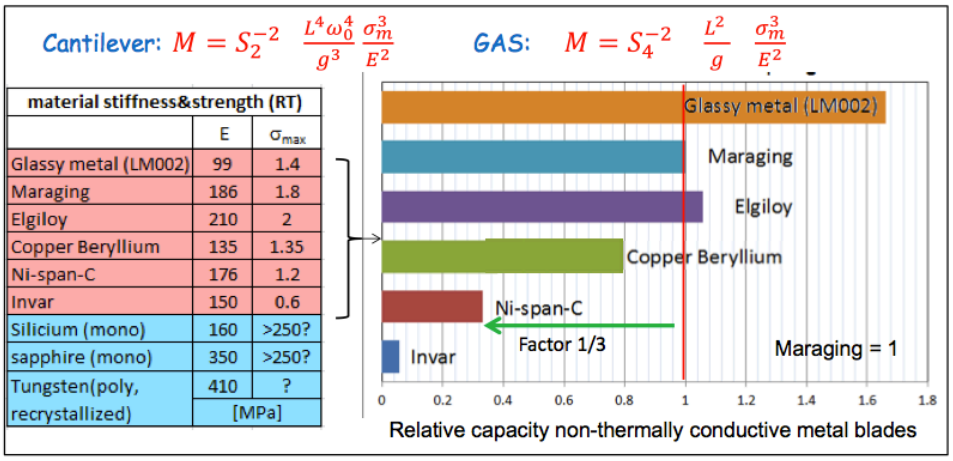

Figure 56: *Load capacity of blade spring of shape factor S, size L, frequency ω_0 for several metals.*

panel) that the nominal load curve (green) shifts towards a larger mass load (blue line) by 100 grams/K, when the filter is tuned to 235 mHz.

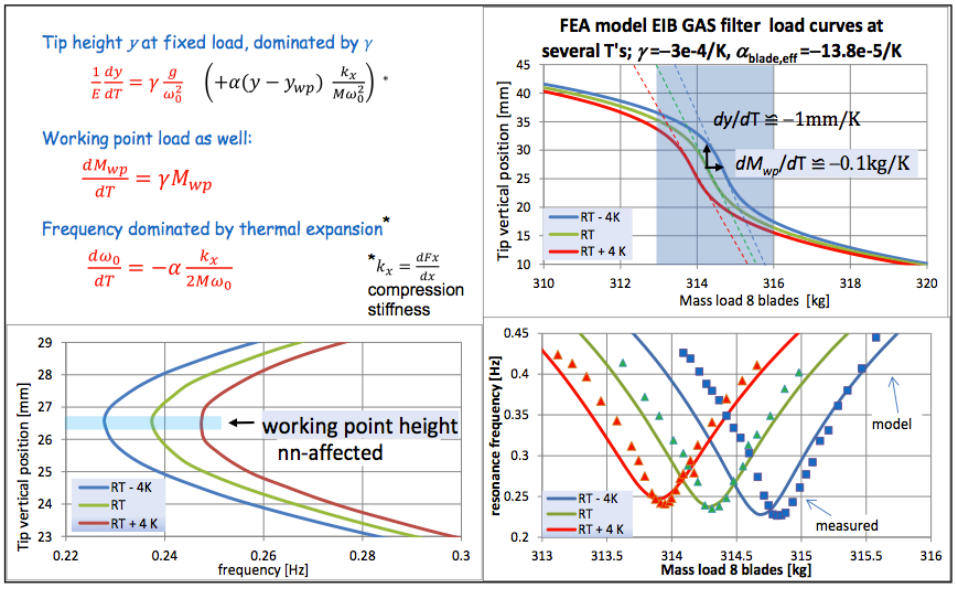

Figure 57: *Maraging GAS blade spring response to small thermal fluctuation, close to working point. An aluminum support plate, as in EIB–SAS is assumed.*

This means that, for a constant mass load, the mass moves upward, in this case by 1 mm/K. This is mainly due to the increased stiffness of the maraging blades. Moreover, the load curve steepness has slightly increased,

resulting in a lower resonance frequency. Apparently the blades feel more compression, which is explained by the relative thermal contraction between the aluminum filter plate and the maraging steel GAS blades. Finally, note that the working point height is unaffected by the change in temperature.

6.2.3 Cooling a GAS filter down to 10 K

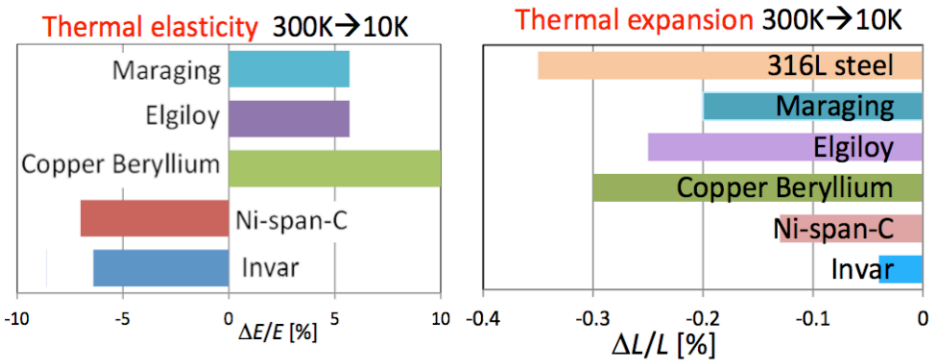

Figure 58: *Young modulus variation and thermal contraction down to cryogenic temperature for several metals.*

Effect of thermoelasticity Fig. 58 shows that maraging steel is about 5.7% stiffer at 10 K, compared to room temperature. As a consequence, the keystone of a loaded maraging GAS filter tuned at room temperature will move upward until it reaches its end–stop. Bringing the suspended mass back into its working point after cool down appears to be quite challenging. The options are:

- the simplest way would be to add the 5.7% missing mass (several kg in KAGRA) to the payload and retune the filter to some precision but this is very impractical;
- combining maraging and Nispan–C (which has opposite thermoelastic behavior) blades. However, Nispan-C has only 1/3 of the loading capability of maraging, so that 3 Nispan–C blades would be needed to compensate one maraging blade.
- preloading the GAS filter with the needed additional mass, such that it will reach its working point at 10 K. The filter will then be disabled at room temperature.

The last mentioned approach looks the most viable even if, due to the required very high pre–loading accuracy, reaching very low natural frequencies

looks hardly achievable. However, working around 0.5–1 Hz could be feasible. A complication may arise if the filter body compliance plays a significant role in the GAS spring mechanics. In that case the deformation of the body, due to the large torques and forces acting on it, affect the filter's tuning properties. After cooling down, its increased stiffness detunes the filter.

Effect of thermal contraction If the GAS filter blades and the filter body on which the blades are clamped are made of different materials (see Fig. 58), then their thermal contraction at low temperatures affects the compression state of the system. For instance, the usual combination of maraging steel blades mounted on a stainless steel plate will get over-compressed. Solutions to prevent that are decompressing the system at room temperature, and hopefully end up at the desired frequency at 10 K, or, more practically, using for the filter baseplate a material with the same expansion coefficient as the blades.

7 Summary

KAGRA–SAS, being just an upgrade of the successful Virgo superattenuators, will deliver a guaranteed seismic attenuation in excess to KAGRA's requirements. The main performance limitation may come from the heat links between the cryostat and the cryogenic mirror. Suitable isolation techniques are being developed to mitigate this problem. Mono-crystalline suspensions are being developed to both support and refrigerate the cryogenic mirrors. The new features first implemented in KAGRA, dual tunnel solution with long suspension wires, eddy current damping of internal modes, will serve as path opener for the third generation Gravitational Wave Detectors like the Einstein Telescope.

References

[1] M.Punturo and K.Somiya. Underground gravitational wave observatories: KAGRA and ET. *Int.J.Mod.Phys.D*, **22**:1330010, 2013. 1

[2] R.DeSalvo. Type-B suspension drawings, 2013. KAGRA document JGW-D1201181, http://gwdoc.icrr.u-tokyo.ac.jp/. 1, 4

[3] R.DeSalvo. Design of the Type-A seismic attenuation, 2013. KAGRA document JGW-D1200904, http://gwdoc.icrr.u-tokyo.ac.jp/. 1, 4

[4] R.Takahashi *et al.* Vacuum-compatible vibration isolation stack for an interferometric gravitational wave detector TAMA300. *Rev. Sci. Instrum.*, **73**:2428, 2002. 1

[5] T.Accadia *et al.* VIRGO: a laser interferometer to detect gravitational waves. *JINST*, **72**:P03012, 2012. 2, 45

[6] K.Arai *et al.* Status of Japanese gravitational wave detectors. *Class.Quant.Grav.*, **26**:204020, 2009. 2

[7] G.Ballardin *et al.* Measurement of the VIRGO superattenuator performance for seismic noise suppression. *Rev. Sci. Instrum.*, **72**:3643, 2001. 2

[8] R.Takahashi *et al.* Operational status of TAMA300 with the seismic attenuation system (SAS). *Class.Quant.Grav.*, **25**:114036, 2008. 4

[9] S.Marka *et al.* Anatomy of the TAMA SAS seismic attenuation system. *Class.Quant.Grav.*, **19**:1605, 2002. 4

[10] G.Cella *et al.* Seismic attenuation performance of the first prototype of a geometric anti-spring filter. *NIM A*, **487**:652, 2002. 4

[11] T.Sekiguchi. Modeling and simulation of vibration isolation system for large-scale cryogenic gravitational-wave telescope (lcgt). Master's thesis, University of Tokyo, 2012. KAGRA document JGW-P1200770, http://gwdoc.icrr.u-tokyo.ac.jp/. 5, 19, 47

[12] R.DeSalvo and F.Raffaelli. Finite Element Model analysis of External Frame for tower B1 and B2, 2013. KAGRA document JGW-T1201363, http://gwdoc.icrr.u-tokyo.ac.jp/. 4

[13] A.Wanner *et al.* Seismic attenuation system for the AEI 10 meter Prototype. *Class.Quant.Grav.*, **29**:245007, 2012. 4, 25

[14] M.R.Blom *et al.* Seismic attenuation system for the external injection bench of the Advanced Virgo gravitational wave detector. *NIM A*, **718**:466, 2013. 4

[15] A.Bertolini *et al.* MultiSAS technical readiness review report - Rev.01, 2013. VIRGO note VIR-0130A-13, https://tds.ego-gw.it/itf/tds/. 4

[16] A.Bertolini *et al.* Seismic noise filters, vertical resonance frequency reduction with geometric anti-springs: a feasibility study. *NIM A*, **435**:475, 1999. 4

[17] G.Cella *et al.* Monolithic geometric anti-spring blades. *NIM A*, **540**:502, 2005. 6

[18] A.Stochino *et al.* Improvement of the seismic noise attenuation performance of the Monolithic Geometric Anti-Spring filters for gravitational wave interferometric detectors. *NIM A*, **580**:1559, 2007. 7

[19] A.Stochino *et al.* The Seismic Attenuation System (SAS) for the Advanced LIGO gravitational wave interferometric detectors. *NIM A*, **598**:737, 2009. 11, 12, 26

[20] G.Losurdo *et al.* An inverted pendulum preisolator stage for the VIRGO suspension system. *Rev. Sci. Instrum.*, **70**:2507, 1999. 11

[21] R.DeSalvo. Dual tunnel seismic isolation, 2010. KAGRA document JGW-T1000251, http://gwdoc.icrr.u-tokyo.ac.jp/. 16

[22] L.Carbone *et al.* Sensors and actuators for the Advanced LIGO mirror suspensions. *Class.Quant.Grav.*, **29**:115005, 2012. 21, 40

[23] H.Tariq*et al.* The linear variable differential transformer (LVDT) position sensor for gravitational wave interferometer low-frequency controls. *NIM A*, **489**:570, 2002. 22

[24] C.Wang*et al.* Constant force actuator for gravitational wave detector's seismic attenuation systems (SAS). *NIM A*, **489**:563, 2002. 22

[25] A.Bertolini*et al.* Mechanical design of a single-axis monolithic accelerometer for advanced seismic attenuation systems. *NIM A*, **556**:616, 2006. 22

[26] Jo van den Brand et al. EIB-SAS performance document draft, 2011. VIRGO note VIR-0578B-11, https://tds.ego-gw.it/itf/tds/. 24

[27] R.DeSalvo *et al.* The role of Self-Organized Criticality in elasticity of metallic springs: observations of a new dissipation regime. *Eur.Phys.J.Plus*, **126**:75, 2011. 26

[28] R.DeSalvo *et al.* Study of quality factor and hysteresis associated with the state-of-the-art passive seismic isolation system for Gravitational Wave Interferometric Detectors. *NIM A*, **538**:526, 2005. 26

[29] M.Mantovani *et al.* One hertz seismic attenuation for low frequency gravitational waves interferometers. *NIM A*, **554**:546, 2005. 26

[30] Y.Arase *et al.* Damping system for torsion modes of mirror isolation filters in TAMA300. *J.Phys: Conf.Ser.*, **122**:012027, 2008. 32

[31] The Virgo collaboration. Adanced Virgo Technical Design Report, 2012. VIR-0128A-12, https://tds.ego-gw.it/itf/tds/. 45

[32] T.Sekiguchi. Control servo design for inverted pendulum, 2014. KAGRA document JGW-T1402132, http://gwdoc.icrr.u-tokyo.ac.jp/. 49, 54

[33] T.Sekiguchi. Type-A SAS Mechanical Model Parameters, 2013. KAGRA document JGW-T1302090, http://gwdoc.icrr.u-tokyo.ac.jp/. 49

[34] E.Hirose and T.Sekiguchi. Preliminary design of Type–A suspension system for KAGRA sapphire mirrors, 2014. KAGRA document JGW-T1402106, http://gwdoc.icrr.u-tokyo.ac.jp/. 49, 56

[35] P.Ruggi G.Losurdo, D.Passuello. The control of the Virgo Superattenuator revised (I). Inertial damping: present and future, 2006. VIRGO note VIR–NOT–FIR–1390-318, https://tds.ego-gw.it/itf/tds/. 52

[36] R.DeSalvo. Dimensioning the cryo suspension, 2013. KAGRA document JGW-G1201312, http://gwdoc.icrr.u-tokyo.ac.jp/. 56

[37] D.Chen. Study of radiation shield vibration in KAGRA cryostat, 2013. KAGRA document JGW-G1302049, http://gwdoc.icrr.u-tokyo.ac.jp/. 57

[38] F.Frasconi *et al.* A vertical accelerometer for cryogenics implementation in third-generation gravitational-wave detectors. *Meas. Sci. Technol.*, **25**:015103, 2014. 57

[39] E.Hennes. The issue of vertical filters in cryogenic environment, 2013. talk at 2^{nd} ELiTES General Meeting, 4-5 December, Tokyo, available from http://www.et-gw.eu/. 57